The loss of V0-ATPase induces Microvillus inclusion-like disease in *C. elegans*

Aurélien Bidaud-Meynard[1], Ophélie Nicolle[1], Markus Heck[1] and Grégoire Michaux[1, *]

Univ Rennes, CNRS, IGDR (Institut de Génétique et Développement de Rennes) - UMR 6290, F-35000 Rennes, France

* lead contact gmichaux@univ-rennes1.fr

Short title: V0-ATPase depletion causes MVID in *C. elegans*

Summary

Food absorption relies on the strong polarity of intestinal epithelial cells and the array of microvilli forming a brush border at their luminal pole. Recent discovery of the genes associated with rare genetic absorption disorders such as Microvillus inclusion disease (MVID) enlightened a major role of membrane trafficking in the maintenance of both the enterocyte polarity and the integrity of the brush border. However, how membrane trafficking defects can lead to food malabsorption in MVID patients is still poorly understood. Combining genetic RNAi screen and *in vivo* super-resolution imaging in *C. elegans* intestine, we uncovered that depletion of the V0 sector of the V-ATPase (V0-ATPase) fully recapitulates the severe structural, polarity and trafficking defects observed in enterocytes from patients with MVID. Furthermore, we show that V0-ATPase specifically controls an apical trafficking step involving RAB-11 endosomes and the SNARE SNAP-29. Finally, this new *in vivo* MVID model allowed to follow the dynamics of microvillus inclusions and to characterize the potential rescue of MVID phenotype by cholesterol complementation. Hence, we describe a new function for the V0-ATPase in apical trafficking and epithelial polarity maintenance and the promising use of *C. elegans* intestine as an *in vivo* model to better understand the molecular mechanisms of rare genetic enteropathies.

Author Summary

Maintenance of the strong polarity of intestinal epithelial cells and the array of microvilli forming a brush border at their luminal pole is essential to food absorption. Recent studies on rare genetic absorption disorders such as Microvillus inclusion disease (MVID) identified a major, albeit ill-defined, role of membrane trafficking in the maintenance of both the enterocyte polarity and the integrity of the brush border. Combining systematic depletion of trafficking genes by RNAi and *in vivo* super-resolution imaging in *C. elegans* intestine, we uncovered that depletion of the V0 sector of the V-ATPase complex (V0-ATPase) fully recapitulates the severe structural, polarity and trafficking defects observed in enterocytes from patients with MVID. Using this new *in vivo* MVID-like model, we characterized a new pathway of polarity maintenance, studied the dynamics of microvillus inclusions as well as identified the potentcy of cholesterol complementation to correct V0-ATPase depletion-induced polarity and structural defects. Thus, we describe here both a new cellular function of the V0-ATPase and a new *in vivo* model to study the mechanisms of MVID.

Introduction

Considering that almost all nutrients in the diet are absorbed into blood across the epithelial layer forming the small and large intestinal mucosa (1), proper establishment and maintenance of both the strong polarity of enterocytes and the array of microvilli forming an absorptive brush border at their apical plasma membrane (PM) are essential to ensure intestinal functions. In most species, including *C. elegans*, epithelial cell polarity is achieved by actin and microtubule cytoskeleton reorganization, trafficking and signaling-mediated polarized targeting of the CDC-42/PAR-3/PAR-6/PKC-3 (CDC-42/PAR) and Crumbs/PALS1/Patj (CRB) modules at the apical pole and the Dlg/Scribble/Lgl (SCRIB) module at the basolateral pole as well as domain-specific lipid distribution (2). Particularly, CDC-42 has been shown to be a major player of polarity maintenance in *C. elegans* by controlling the apico-basal distribution of PAR proteins (3, 4). The establishment of the brush border, an extended PM surface for efficient nutrient uptake, is thought to be highly dependent on actin cytoskeleton regulating factors which create the force necessary for the onset and maintenance of the microvilli (5-8). Polarity establishment and brush border formation are early events in intestine development that both rely on related trafficking pathways (9-11), glycosphingolipids (GSLs) (12), clathrin and AP-1 (3, 13) and the kinase Lats/WTS-1 (14). However, little is known about their sequential involvement and relationship in establishing and maintaining an absorptive apical PM, especially *in vivo*.

Interestingly, recent studies on rare genetic absorption diseases enlightened a major role of membrane trafficking in the maintenance of both enterocyte polarity and brush border (15). For instance, Microvillus inclusion disease (MVID, OMIM: 251850) is caused by mutations in the genes coding for myosin-5B (MYO5B) (16), syntaxin-3 (STX3) (17) or Munc18-2/STXBP-2 (STXBP2) (18), three proteins regulating apical trafficking. The major hallmarks of this disease are a microvillus atrophy, the rare formation of microvillus inclusions, as well

as a loss of subapical RAB-11^{+} endosomes (15). Additionally, we have recently shown that enterocytes from MVID patients also display a mispolarized CDC-42/PAR polarity module (19). At the molecular level, a defective apical PM tethering of RAB-8^{+}/RAB-11^{+} endosomes by Myosin 5B (20) in concert with STX3 (11) and Munc18-2 (18) has been proposed to be the major pathway leading to MVID phenotype (21). However, the molecular mechanism by which these membrane trafficking factors control the integrity of the absorptive apical PM and the other components of this pathway are still unknown. This lack of knowledge may be explained by the fact that essential factors required to build the intestinal apical PM are cytoplasmic proteins, not transported through membrane trafficking *per se*, and by the difficulty to conduct *in vivo* studies in the intestine.

C. elegans intestine is composed of 20 polarized enterocytes similar to that of mammalian cells (22) and the nematode embryonic and larval stages have been widely used to understand polarity and lumen establishment (23) and maintenance (24), respectively. By performing an RNAi screen to target a library of trafficking and cytoskeleton factors in *C. elegans* larvae, we unveiled that the depletion of the V0 sector of the vacuolar-ATPase (V-ATPase) induces a cytoplasmic and basolateral mislocalization of both PAR polarity module and brush border components. The V-ATPase is a large hetero-multimeric complex (20 subunits in *C. elegans*, *vha-1* to *vha-18*, *spe-5* and *unc-32*), organized in two main sectors: a V1 sector responsible for ATP hydrolysis which provides the energy to the V0 sector, which transports protons (25). The whole V-ATPase complex is responsible for the acidification of intracellular compartments, such as endosomes or lysosomes and plays a major role in PM proteins trafficking (26), while its V0 transmembrane sector (V0-ATPase) has been implicated in the fusion to the yeast vacuole (27) as well as that of synaptic vesicles in drosophila and humans (28, 29), in an acidification-independent manner. In *C. elegans*, the V0-ATPase subunits *vha-5*, *vha-6* and *vha-19* are required for exosome containing vesicle apical exocytosis

in the epidermis (30), intestinal lumen pH regulation (31) and RME-2 receptor trafficking in oocytes (32) but no role in polarity maintenance has been assigned to this complex. In this study, we describe a new role for the V0-ATPase in apical membrane trafficking necessary for intestinal polarity maintenance and show that depletion of this complex leads to an MVID-like phenotype in *C. elegans*.

Results

V0-ATPase depletion affects the polarity of brush border and polarity components in the *C. elegans* intestine

To identify new common regulators of polarity and brush border maintenance *in vivo*, we performed a two-step RNAi screen specifically targeting 408 genes conserved in humans and implicated in membrane trafficking and cytoskeleton regulation. First, we examined the effect of their silencing on the localization of the polarity module component CDC-42 at the apical PM of enterocytes of *C. elegans* larvae. Then, we performed a secondary screen to evaluate the ability of the hits decreasing CDC-42 apical localization to also disturb the polarity of the brush border specific actin cross-linker ERM-1 (S1 Table and S1 Fig A). This systematic RNAi screen first confirmed the involvement of clathrin (*chc-1*), AP-1 (*aps-1*) and glycosphingolipids (GSLs) biosynthesis enzymes (i.e. *sptl-1*, *fasn-1*, *pod-2*) (3, 13, 33) in the maintenance of intestinal polarity (S1 Table) and identified several genes belonging to the biosynthetic and endocytic pathways, as well as 10 subunits of the V-ATPase complex, a major player of intracellular trafficking by regulating endosomal acidification (S1 Table). This screen was then confirmed by silencing several subunits of the V-ATPase complex and studying the endogenous localization of genome-edited mNeongreen or GFP-tagged ERM-1 as well as the polarity module components PAR-6 and PKC-3. Consistently, knockdown of all the V-ATPase complex subunits decreased by 15-40% the apical/cytoplasmic ratio of the PAR module proteins, while silencing of subunits of the V0 sector of the complex (V0-ATPase) decreased more the Ap/cyto ratio of ERM-1 than that of V1 sector subunits (V1-ATPase) (Fig 1A-F). This indicates that a V-ATPase acidification-dependent mechanism is involved in the apical confinement of brush border and polarity module components. Intriguingly, depletion of the subunits *vha-1*, *-4* and *-19*, belonging to the V0-ATPase also induced a basolateral localization of ERM-1, while no basolateral mislocalization was observed upon silencing of the V1-ATPase

subunits *vha-8* and *-15* (Fig 1A, G). Furthermore, PAR-6 and PKC-3 could also be specifically observed at the basolateral PM in ~20% of the enterocytes upon V0-ATPase subunits depletion (Fig 1B). To evaluate if V0-ATPase silencing induces a global polarity inversion of the enterocytes we studied the effect of the silencing of the V0-ATPase subunit *vha-1*, which destabilizes the whole V0-ATPase sector (S1 Fig, B-C) and the V1-ATPase *vha-8*, which has been shown to inhibit V-ATPase-dependent acidification (34), on the polarized localization of the apical peptide transporter PEPT-1 (OPT-2) and the P-glycoprotein PGP-1 as well as the basolateral pyruvate transporter SLCF-1. Notably, silencing of subunits from both complexes did not induce a significant effect on the cortical confinement of the PM transporters PEPT-1 and SLCF-1 (Fig 1H, J, S2A), while the apical level of the P-glycoprotein PGP-1 was increased upon V1-ATPase silencing (Fig 1I, K), suggesting that its cellular fate partly depends on a V-ATPase dependent lysosomal degradation, as shown before for the P-glycoprotein ABCB1 in mammalian cells (35). Notably, none of these highly polarized proteins accumulated at the contralateral PM (Figs 1H-I), supporting the notion that the enterocyte polarity is only partially compromised upon V0-ATPase depletion. Overall, these data indicate that the V0-ATPase sector specifically controls the polarized localization of both brush border (ERM-1) and polarity module components (PAR-6, PKC-3) in enterocytes, which is consistent with previous studies demonstrating an acidification-independent function of this complex (27-30).

V0-ATPase depletion specifically affects the apical recycling pathway

The V-ATPase complex controls the acidification of various endosomes along the biosynthetic and endocytic-recycling routes (36). Using Transmission Electron Microscopy (TEM), we observed the presence of abnormal large organelles (0.1–0.3 μm in diameter with variable electron density and heterogeneous content) with features of vesicles, lysosomes and autophagosomes upon inhibition of both V0 and V1-ATPase subunits (Fig 2A-B). These

"mixed" organelles have been already described in the *C. elegans* epidermis and in mammalian cells upon V0-/V1-ATPase silencing or chemical inhibition of the V-ATPase complex function, and have been proposed to affect protein sorting along the secretory and lysosomal pathways (30, 37), probably due to an endosome acidification failure. The presence of mixed organelles was confirmed by the accumulation of several endosomal markers in large cytoplasmic structures, such as LMP-1 (lysosomes), RAB-7 (late endosomes) and RAB-10 (basolateral recycling endosomes) (Figs 2C and S2B), upon both V0-and V1-ATPase silencing.

Strikingly, V0- but not V1-ATPase depletion led to the specific accumulation of electron-lucent vesicular structures in the cytoplasm (Fig 2D), which were reminiscent of an apical trafficking defect. Moreover, the number of RAB-5^{+} endosomes was slightly decreased (Fig 2E-F) while RAB-11 virtually disappeared from the apical PM and accumulated in the cytoplasm upon V0- but not V1-ATPase knockdown (Fig 2G-H). Considering that *rab-11* knockdown also induced a basolateral mislocalization of ERM-1 (Fig 2I-J), similarly to *vha-1(RNAi)* (Fig 1B, G) this indicates that V0-ATPase controls the enterocyte polarity by regulating a protein recycling step through RAB-11^{+} endosomes.

SNAP-29 is involved in V0-ATPase-mediated polarity maintenance

To identify some of the molecular components of this V0-ATPase-mediated control of intestinal polarity beyond the interaction with RAB-11, the effect of V0- or V1-ATPase depletion was assayed on several soluble trafficking factors with a highly polarized expression. The PM localization of CHC-1/clathrin and the syntaxin SYX-1 (SYN-1) was decreased (Figs 2A and S2C), while that of the syntaxin UNC-64 (the presumptive mammalian STX3 ortholog) was increased (Fig 3B) upon all V-ATPase complex subunits depletion, suggesting a trafficking defect, but no sector-specificity. Strikingly, *vha-1/V0-ATPase(RNAi)* specifically decreased the apical localization of the soluble N-ethylmaleimide-sensitive factor-attachment

protein receptors (SNAREs) component SNAP-29, while *vha-8/V1-ATPase(RNAi)* did not (Fig 3C). SNAP-29 belongs to the SNAP23/25/29 family of SNARE proteins that interact with syntaxins and sec/munc proteins to promote vesicle fusion (38). Its depletion has been shown to affect the morphology of various organelles, including recycling endosomes, and consequently endocytosis, secretion as well as autophagy pathways in *C. elegans* intestine (39, 40). To test whether SNAP-29 is involved in polarity maintenance, *snap-29* was silenced by RNAi (S2 Fig, D-E) and the PM localization of ERM-1 was assessed. *snap-29* silencing induced a basolateral mislocalization of ERM-1 (Bl/cyto ratio >1.5) in 44.3% of the worms whereas only 20.8% of control (L4440) worms displayed a ratio >1.5 (Fig 3D-E). Hence, these data indicate that SNAP-29 acts downstream of the V0-ATPase to maintain the enterocyte polarity.

High-resolution map of the apical PM revealed that V0-ATPase localizes to microvilli

The V0-ATPase has been localized at the apical PM of intestinal epithelia in *C. elegans* (41) and proposed to traffic to the brush border in Caco-2 cells (42). However, conventional confocal imaging in *C. elegans* only allowed to determine the apical polarity of markers, but not their precise position regarding the apical PM (e.g. microvilli, terminal web, subapical). The precise localization of the V0-ATPase as well as that of some of the above-mentioned polarity markers was thus assessed by live super-resolution confocal microscopy. This technique confirmed that ERM-1 accumulates in the microvilli, while ACT-5, PGP-1 and SNAP-29 were present at both the microvilli and the underlying terminal web (Fig 3F). SNAP-29 has been previously shown to localize on RAB-11^{+} endosomes in *C. elegans* intestine (43), and this interaction seems to take place at the presumptive terminal web level (Fig 3F), where the PAR component PKC-3 mostly accumulates. Finally, the V0-ATPase subunit VHA-6 was localized to the microvilli, above the RAB-11 apical staining (Fig 3F). Overall, these results

strongly suggest that the V0-ATPase localizes at microvilli from where it controls the apical localization of brush border and polarity modules by regulating a protein recycling step through RAB-11^{+} endosomes in a SNAP-29-dependent manner.

V0-ATPase depletion phenocopies MVID

Next, we asked whether the polarity defects associated with V0-ATPase depletion were associated with brush border structural defects. Combined TEM and super-resolution imaging demonstrated that prolonged V0-ATPase depletion (72 and 96h of *vha-1(RNAi)*) specifically induced a microvillus atrophy, with smaller, thinner or even absent microvilli at the apical PM of enterocytes (Fig 4A-C). Conversely, V1-ATPase depletion (*vha-8(RNAi)*), despite inducing a decreased worm size and a mild decrease of microvilli length, did not affect the microvilli structure and organization (Figs 4A-C and S3A). The severe apical PM defect induced by V0-ATPase depletion was observed along the whole surface of the deformed lumen and was often associated with a local unhooking of microvilli membrane from the underlying cytoskeleton (S3 Fig, B) as well as slightly lengthened adherens junctions (CeAJs) (S3 Fig, C-D). Thus, V0-ATPase depletion specifically leads to severe apical PM structural defects, which may affect the absorptive function of the enterocytes, in line with the luminal accumulation of cellular or bacterial debris and the absence of yolk storage granules observed in *vha-1(RNA)* but not *vha-8(RNAi)* worms (S3 Fig, E-F). In addition to these apical PM defects, super-resolution microscopy showed that the brush border components ACT-5 and ERM-1 adopt a pattern reminiscent of microvilli when mislocalized to the basolateral PM (Fig 4D-E) although TEM analysis did not reveal the presence of *bona fide* microvilli.

Surprisingly, prolonged V0-ATPase depletion lead to the accumulation of rounded ERM-1^{+} and ACT-5^{+} structures (Fig 5A-B), which displayed a microvilli-like pattern on higher magnification (Fig 5C) and closely resemble cytoplasmic microvillus inclusions (MVIs)

observed in MVID patients (44) and in *STXBP2* KO organoids MVID model (45). These structures are also enriched in PKC-3 and SNAP-29 (Fig 5D-E). TEM experiments performed on *vha-1* depleted worms confirmed the presence of typical MVIs lined by inward-pointing microvilli (Fig 5F). We also observed many vacuole-like structures with a wide size (0.1–0.6 μm in diameter), shape and electron-density heterogeneity and containing cellular material (Fig 5G). These vacuole-like structures were positive for the microvilli-specific activated phospho-form of ezrin, as observed by immuno-EM (Fig 5H) and are similar to the already described "irregular" MVIs that are probably immature or degrading MVIs (44). Strikingly, microvillus atrophy and MVIs are cellular hallmarks of Microvillus inclusion disease (MVID, OMIM: 251850), a congenital disorder of intestinal epithelial cells (46) caused by mutations in the genes coding for the trafficking proteins Myosin 5B (MYO5B) (16), Syntaxin3 (STX3) (17) or Munc18-2 (STXBP2) (18). Interestingly, enterocytes of patients with MVID also displayed similar polarity defects than that observed upon *vha-1(RNAi)*, such as the basolateral appearance of microvilli-specific proteins (17), the basolateral mislocalization of PAR polarity module components (19) as well as the cytoplasmic displacement of trafficking (i.e. STX3, the SNAREs family component SNAP23 and cellubrevin) (21) proteins. Finally, MVID has also been associated with enlarged lysosomes displaying a heterogeneous content (Fig 2A, C) and with the accumulation of subapical translucent vesicles (Fig 2D) (44, 47) as well as the specific disorganization of Rab11^{+} apical recycling endosomes (Fig 2G-H) (48, 49). These and other observations strongly suggest that V0-ATPase depletion in *C. elegans* fully recapitulates the defects observed in the enterocytes of patients suffering from MVID and MVID *in vitro* mammalian models (S2, S3 Tables) (45).

Study of MVIs dynamics in *C. elegans* model

Using live microscopy in intestinal organoids derived from *STXBP2* knock-out mouse, we recently contributed to show that MVIs can arise *de novo* in the cytoplasm or by internalization of both the apical and the basolateral PM (45). To test whether these various modes of MVI onset are conserved in *C. elegans* upon V0-ATPase depletion, we performed live imaging on endogenously expressed ERM-1::mNG after 96h of *vha-1(RNAi)*. This experiment confirmed that MVI-like structures can rapidly nucleate in the cytoplasm (~3 min) and remained in the cytoplasm from less than 3 min to more than 1h (Fig 6A and S1-S2 Movies), a process that may involve lysosomal remodelling (45). These structures also arise by internalization of large ERM-1::GFP$^+$structures from the apical and basolateral PM of *vha-1* depleted worms (Fig 6B, S4 Fig and S3 Movie), which has been linked to an autophagocytic process (50). Since autophagosomes and lysosomes have been linked to MVIs, we hypothesized that these structures undergo a cytoplasmic elimination through these degradation pathways. Consistently, live tracking of MVIs in *STXBP2* KO organoids revealed that MVIs are often surrounded by LAMP2$^+$ membranes and mostly disappear by cytoplasmic desintegration (67,5%) while the rest was eliminated by PM fusion or cell shedding (45). Interestingly, we found that irregular MVIs induced by *vha-1(RNAi)* were often in close proximity to mixed organelles/lysosomes (Fig 6C) and that some of the ERM-1$^+$ MVIs were also positive for the lysosomal marker LMP-1 (Fig 6D). Furthermore, some MVIs were also surrounded by a second membranous layer positive for ERM-1 (Fig 6E). Considering that i) ezrin has been shown to accumulate at the phagosome membrane and regulate phago-lysosomal fusion (51) and ii) V0-ATPase extinction dramatically activates autophagy, as ascertained by the relocalization of LGG-1::GFP (LC3 *C. elegans* ortholog) from the apical PM to cytoplasmic punctaes (Fig 6 G-H) (52), these data strongly suggest that MVIs are eliminated by autophagosomes and/or lysosomes in *C. elegans* intestine, as proposed in mammals. This was confirmed by timelapse microscopy on ERM-1$^+$ MVIs, which

progressively disintegrated in the cytoplasm or inside ERM-1^{+} secondary structures (Fig 6F and S4 Movie).

V0-ATPase depletion-induced MVID-like phenotype can be partly rescued by cholesterol supplementation

Most of the lipids in *C. elegans* intestine are stored in electron-translucent comportments called lipid droplets, while cholesterol accumulates in lysosome-related organelles (LROs), also called gut granules (53, 54). Notably, a lipid storage defect has been observed in *goosepimples/myosin5b* zebrafish mutants (55) and could be reminiscent of lipids and other nutrients absorption defects, as observed in MVID patients. Interestingly, V-ATPase knockdown in HeLa cells has been proposed to affect clathrin-mediated endocytosis by inhibiting cholesterol recycling, a phenomenon that was rescued by cholesterol supplementation (56). Hence, the trafficking defects due to V0-ATPase depletion could create a cholesterol imbalance in the brush border that would lead to MVID-like structural and polarity phenotypes which may be rescued by cholesterol supplementation. To test this conjecture, V0-ATPase depleted worms were cultured on NGM plates supplemented with normal (5 μg.ml-1) or high (50 μg.ml-1) cholesterol concentration. Notably, the microvilli structural defects (Fig 7A) and ERM-1 basolateral mislocalization (Fig 7B) associated with *vha-1* silencing were partly rescued in high-cholesterol compared to control condition. Hence, the MVID-like phenotype induced by V0-ATPase depletion can be partially rescued by cholesterol supplementation, which suggests that a lipid homeostasis defect in the brush border may contribute to the polarity and structural defects observed in patients suffering from this disease.

Discussion

By performing a double-RNAi screen in *C. elegans* intestine model we identified a new function of the V0-ATPase complex as a critical determinant for the maintenance of one of the most prominent cell surfaces, the absorptive apical PM of the enterocytes. Our results demonstrate that the V0-ATPase ensures the apical localization of polarity modules, brush border component and trafficking factors, a major role that is substantiated by the severe brush border defects consecutive to V0-ATPase depletion.

This study confirms the biological significance of systematic RNAi screens in *C. elegans* to understand the complex mechanisms of polarity maintenance. Indeed, this model has allowed to characterize the major role of membrane trafficking factors in epithelial polarity maintenance including GSLs (33), clathrin and its adpator AP-1 (3, 13) and the interactions between polarity proteins and membrane trafficking (24, 57). Particularly, these studies highlighted the central role of RAB-11-dependent apical trafficking in polarity maintenance ((3, 24) and Fig 2). Accordingly previous studies demonstrated the critical role of RAB-11^+/RAB-8^+ endosomes in apical PM and lumen generation by mediating PAR-3 targeting and CDC-42 activation through the exocyst complex (58, 59), as well as the adverse effect of dominant-negative Rab11 expression on the apical polarity of phospho-ezrin and E-Cadherin in MDCK cells (60). Intriguingly, while interfering with Clathrin/AP-1, PAR-5 or GSLs pathways induced a RAB-11^+ endosomes loss and an inversion of both apical and basolateral PM proteins polarity (3, 13, 24, 33), we showed here that V0-ATPase silencing has a specific effect on brush border and CDC-42/PAR polarity but not on transmembrane or basolateral proteins (Figs 2, 3). This surprising result points to a specific role of V0-ATPase in late trafficking events, downstream of sorting factors such as GSLs, clathrin and AP-1. This conclusion is supported by the known function of V0-ATPase in vesicle fusion to the plasma membrane, by the accumulation of subapical vesicles, and by the phenotypic similarities with

the loss of Myosin 5B, STX3 or Munc18-2 in patients; indeed all these factors have been found to control late trafficking events just upstream of the fusion to the apical membrane. In summary clathrin/AP-1 (3, 13), GSLs (13, 33) or the kinase Lats/WTS-1 (14) might control sorting events, inducing lateral to apical conversion, while V0-ATPase, Myosin 5B, STX3 or Munc18-2 would control late trafficking steps, inducing MVI formation (S4 Fig).

The precise mechanism by which the V0-ATPase controls the maintenance of the intestinal polarity remains to be elucidated. The most studied function of this complex in membrane trafficking relies on the H^+-pump-dependent (V0+V1 subunits) acidification of intracellular organelles, which ensures their maturation and transport capacity (26). However, our results demonstrated a specific requirement for the V0-sector of the V-ATPase complex in polarity maintenance, in an acidification-independent manner and likely through its already characterized function in vesicle exocytosis (28, 29). Indeed, the functional relevance of V0-ATPase interaction with the fusion machinery has been demonstrated in many species, such as drosophila or *T. marmorata*, where the V0-a1 subunit (V100 in drosophila) has been shown to interact with the t-SNARE Syx and SNAP25 (28) and with the v-SNARE VAMP-2 (61), respectively. Furthermore, the direct interaction between the V0-c subunit (the ortholog of *vha-1*) and VAMP2 has been shown to be indispensable for efficient synaptic vesicle fusion in mammalian cells (29). A similar mechanism could take place for the apical exocytosis of vesicles containing either polarity and brush border components, which may directly interact with the V0-ATPase (62) and/or apical adaptor proteins, such as the ezrin partner NHERF-1/EBP50 that has been recently found associated with the V-ATPase in interactome studies (62). In line, we found that *vha-1(RNAi)* decreased the apical confinement of the SNARE SNAP-29, a member of the SNAP23/25/29 family (63) which seems to be mislocalized in MVID mammalian models (21), and that *snap-29* extinction phenocopies that of *vha-1* on *C. elegans* intestinal polarity. Considering that SNAP-29 has been localized to RAB-11$^+$

endosomes in *C. elegans* (43), likely at the terminal web (Fig 3) and that mammalian SNAP29 physically interacts with STX3 (63), the V0-ATPase could directly interact with SNAP-29 to target the exocytosis of RAB-11^{+} endosomes and be involved in the same pathway than that of Myosin 5B/STX3/Munc18-2, which may also involve other trafficking factors, such as the N-ethylmaleimide sensitive factor NSF-1/NSF (S1 Table).

Beyond disturbing polarity, we uncovered that V0-ATPase depletion induced severe microvilli defects and the formation of MVIs that are typical features of MVID. MVID is a devastating orphan congenital disorder of intestinal cells that manifested in intractable diarrhoea and intestinal absorption defects appearing in early life of new-borns (46, 64) and therapeutic avenues presently only rely on total parenteral nutrition or small bowel transplantation (64). MVID originates from mutations of MYO5B, STX3 or STXBP2 (21) that belong to the same RAB-11^{+} recycling endosomes apical tethering/fusion machinery: Myosin 5B is a molecular motor that interacts with the syntaxin STX3, and Munc18-2 is a sec/munc family protein that plays an accessory role for STX3-dependent vesicle tethering (21). Hence, MVID is strictly linked to a polarized trafficking defect and *in vitro* mammalian 2D or 3D cell culture models have been developed to study its ill-defined underlying mechanisms, based on Myosin 5B or Rab8/Rab11 depletion and disruption of Myosin 5B-Rab8/11 interaction (20, 65). However, some discrepancies were found while trying to integrate polarity maintenance mechanisms identified *in vitro* and *in vivo*. For instance, while AP-1 was renowned for basolateral sorting in cultured cells (66), its critical role in apical traffic was characterized *in vivo* in *C. elegans* and in mouse (3, 13, 67). While the *in vitro* culture of intestinal organoids derived from MVID patients or MVID causing genes-deficient mouse (15, 17, 45) or the mutation of *myosin5b*/*goosepimples* in zebrafish (55) seem to reproduce most of the cellular and structural hallmarks of MVID, these models are not suitable for systematic studies. Conversely, the *in vivo*, easy-to-use and screening amenable *C. elegans* model has been widely

used to understand intestinal polarity mechanisms (1, 3, 13, 24, 37, 41), but single deletion of the orthologs of MVID-causing genes (i.e. *hum-2*/*MYO5B*, *unc-64*/*STX3*) seems not to induce an MVID phenotype (our unpublished observations), probably due to compensatory mechanisms. We describe here for the first time a *C. elegans* model, V0-ATPase depletion, that fully phenocopies the hallmarks of MVID (S3 Table) and that could be used to better characterize polarity maintenance mechanisms and MVID pathophysiology. As a proof of principle, we studied the dynamics of MVIs, which onset and elimination are still enigmatic. According to the "combined" model of MVI onset (15), in a recent paper using *STXBP2* KO organoids (45) and in the present study (Fig 6), we showed that MVIs may arise by two mechanisms; *de novo* nucleation in the cytoplasm or internalization of the PM. Both may rely on the failure of apical exocytosis from RAB-11^{+} endosomes. Indeed, this defect would on one hand result in the sequestration of polarity factors in the cytoplasm, that may be an upstream signal to target newly-synthesized apical PAR, PM proteins and cytoskeleton and consequently nucleate a new apical PM in the cytoplasm on accumulating vesicles. On the other hand, defective exocytosis may lead to a local apical PM protein/lipid homeostasis defect that would create a signal for endocytosis and targeting to autophagosomal-lysosomal degradation, as proposed before (50) and verified in this report (Fig 6).

Finally, we show that *vha-1(RNAi)* cellular phenotypes can be partly rescued by cholesterol complementation (Fig 7). This advocates that a lipid homeostasis defect, such as the loss of the polarized partition of PI(4,5)P_2 and PI(3,4,5)P_3 between the apical and basolateral PM, respectively (2) or the defective apical enrichment of lipid rafts (68) may be partly responsible for *vha-1(RNAi)*-dependent polarity maintenance impairment. This conjecture is consistent with the major role of the cholesterol-rich lipid rafts as apical sorting platforms (69), which are enriched at microvilli (70), and with the deleterious effect of their chemical disruption or the genetic ablation of GSLs biogenesis on microvilli size in polarized

MDCK cells (71) or luminogenesis in *C. elegans*, respectively (13, 33). Interestingly, the GSLs biogenesis pathway has been shown to genetically interact with Clathrin/AP-1 (13) and leucin-derived monomethyl branched-chain fatty acids (mmBCFAs), while clathrin and AP-1 have been shown to control the apical PM localization of the V0-ATPase subunit VHA-6 (41). Taken together, these data suggest a functional interaction between these polarity maintenance pathways which would be of great interest to characterize. Finally, we provide compelling evidence that V0-ATPase depletion could be involved in the aetiology of MVID (S3 Table) and other absorption disorders associated with apical PM defects. Complementary use of both *C. elegans*, as a tool to screen for correctors of polarity maintenance defects, such as lipid-enriched diet, as well as mammalian intestinal organoids or human samples to confirm the conservation of V0-ATPase function, may lead to a better understanding of the mechanisms of polarity maintenance as well as that of rare genetic enteropathies.

Materials and methods

C. elegans strains and maintenance

Strains were maintained under typical conditions as described (72). When indicated, NGM was supplemented with cholesterol, purchased from Sigma. mNG and mScarlet-tagged ERM-1, UNC-64 and PGP-1 were generated at the « Biologie de *Cænorhabditis elegans* » facility (UMS3421, Lyon, France). The strains used in this study are listed in S4 Table.

Gene silencing and screening by RNAi

Larval RNAi was performed by feeding as described using the Ahringer-Source BioScience library (3, 73). Briefly, adult hermaphrodites were bleached and transferred to RNAi plates containing HT115 E. coli bacteria expressing the L4440 plasmid alone (control) or encoding the RNAi. Developing worms were kept in RNAi for 72-96h before mounting and imaging. RNAi specificity was verified by sequencing and efficiency by target::GFP signal disappearance, as shown in Figures.

in vivo confocal imaging using *C. elegans*

C. elegans imaging was performed *in vivo* by mounting the worms on a 10% agarose pad in a solution of 100 nm polystyrene microbeads (Polysciences Inc.) to stop worm movement. Confocal observations were performed using a Leica (Wetzlar, Germany) SPE equipped with a 63X, 1.4 NA objective (LAS AF software) or a super-resolution Zeiss LSM880 + Airyscan equipped with a 63X, 1.4 NA objective (Zen Black software). All images were examined using Fiji software.

TEM

Control and RNAi worms (72-96 hours) were fixed by high-pressure freezing with EMPACT-2 (Leica Microsystems) and then freeze substituted in anhydrous acetone containing 1% OsO4, 0.5% glutaraldehyde and 0.25% uranyl acetate for 60 h in a freeze substitution system (AFS-2; Leica Microsystems). Larvae were embedded in Epon-Araldite mix (EMS hard formula).

Adhesive frames were used (11560294 GENE-FRAME 65 µL, Thermo Fisher Scientific) for flat-embedding, as previously described (74), to gain better antero-posterior orientation and sectioning. Ultrathin sections were cut on an ultramicrotome (UC7; Leica Microsystems) and were collected on formvar-coated slot grids (FCF2010-CU, EMS). Each larva was sectioned in 5 different places with ≥ 10 µm between each grid to ensure that different cells were observed. Each grid contained at least 10 consecutive sections of 70 nm. TEM grids were observed using a JEM-1400 transmission electron microscope (JEOL, Tokyo, Japan) operated at 120 kV, equipped with a Gatan Orius SC 1000 camera (Gatan, Pleasanton, USA) and piloted by the Digital Micrograph program. Micrographs were analyzed using Fiji software.

Immuno-EM

Immuno-electron microscopy was performed as described (75). For ultrathin cryosections and immunogold labeling, larvae were fixed with 4% paraformaldehyde plus 0.1% glutaraldehyde in M9 buffer. Worms were embedded in 12% gelatin and infused in 2.3 M sucrose. Gelatin blocks were frozen and processed for ultracryomicrotomy (UC7cryo; Leica Microsystems). Ultrathin cryosections (80 nm) were double-immunogold labeled and analyzed by TEM as described above. We applied primary antibodies: rabbit anti-phospho-ezrin (Thr567) / radixin (Thr564) / moes (Thr558) (1/100, 3149S Ozyme), detected using protein A conjugated to 10 nm gold particles (PAG, 1/50, CMC, Utrecht, the Netherlands).

Quantification

Apical/cytoplasmic and basolateral/cytoplasmic ratios were calculated by quantifying the signal intensity on a line covering the width of the apical PM and covering at least the length of 2 adjacent intestinal cells. The intensity of the same line was quantified in the cytoplasm underneath the PM. Basolateral ERM-1 appearance was calculated using the Plot Profile function of Fiji, with a R.O.I. of 1.3 µm long crossing the highest basolateral PM intensity. The 5 highest values were kept and divided by the mean fluorescence of the same R.O.I. in the

cytoplasm. Microvilli length and width were quantified using Fiji on 1) TEM pictures on at least 5 sections per worm (Fig 4) or 2) on confocal pictures by calculating the width of at least 4 lines of >100nm long/image (Fig 7). The number of RAB-5+ vesicles was quantified using a home-made plugin for Fiji, as described (76).

Statistical analysis

Results are presented as mean ± SEM of the number of independent experiments indicated in the legends, and scattered dots represent individual worms. The total number of larvae used is indicated in brackets in histograms. P values were calculated with the means of at least 3 independent experiments by two-tailed unpaired student's t-test and a 95% confidence level was considered significant. Normal distribution of data and homogeneity of variance were validated by calculating the skew factor (-2 > skew < 2) and the F-test, respectively. Mann-Withney U-test and Welch correction were used for calculating the P-values of non-normal and normal distributions with non-homogenous variances, respectively.

Acknowledgements

We thank Verena Gobel, Ken Kemphues, Jeremy Nance, Emily Troemel, Barth Grant and Ken Sato for strains. We also thank the « Biologie de *Cænorhabditis elegans* » facility (UMS3421, Lyon, France) which generated several CRISPR/Cas9 genome-edited strains used in this study. Some strains were provided by the CGC, which is funded by NIH Office of research Infrastructure Programs (P40 OD010440; University of Minnesota, USA). We thank A. Perrin for the initial PAR-6::GFP screen, R. Dima and J. Cailloce for help with screen validation as well as Anne Pacquelet for critical reading of the manuscript and helpful discussions. Imaging was performed at the photonic and electron microscopy facilities of the Microscopy Rennes imaging Center (MRiC), Rennes, France. This work was supported by the Ligue Contre le Cancer Grand Ouest [22/29/35/72/41] and the Fondation Maladies Rares. ABM is the recipient of a postdoctoral fellowship from La Ligue Nationale Contre le Cancer (2017-2018), and a travel grant from the French society for Cell Biology/ITMO BCDE.

Authors contribution

ABM, ON and MH performed and analyzed the experiments. ABM and GM designed the study and wrote the manuscript. GM supervised the study.

Conflict of interest

The authors declare no conflict of interest.

References

1. Kiela PR, Ghishan FK. Physiology of Intestinal Absorption and Secretion. Best Pract Res Clin Gastroenterol. 2016;30(2):145-59.

2. Rodriguez-Boulan E, Macara IG. Organization and execution of the epithelial polarity programme. Nat Rev Mol Cell Biol. 2014;15(4):225-42.

3. Shafaq-Zadah M, Brocard L, Solari F, Michaux G. AP-1 is required for the maintenance of apico-basal polarity in the C. elegans intestine. Development. 2012;139(11):2061-70.

4. Martin-Belmonte F, Gassama A, Datta A, Yu W, Rescher U, Gerke V, et al. PTEN-mediated apical segregation of phosphoinositides controls epithelial morphogenesis through Cdc42. Cell. 2007;128(2):383-97.

5. Heintzelman MB, Mooseker MS. Assembly of the brush border cytoskeleton: changes in the distribution of microvillar core proteins during enterocyte differentiation in adult chicken intestine. Cell Motil Cytoskeleton. 1990;15(1):12-22.

6. Heintzelman MB, Mooseker MS. Structural and compositional analysis of early stages in microvillus assembly in the enterocyte of the chick embryo. Differentiation. 1990;43(3):175-82.

7. Crawley SW, Mooseker MS, Tyska MJ. Shaping the intestinal brush border. J Cell Biol. 2014;207(4):441-51.

8. Saegusa K, Sato M, Sato K, Nakajima-Shimada J, Harada A, Sato K. Caenorhabditis elegans chaperonin CCT/TRiC is required for actin and tubulin biogenesis and microvillus formation in intestinal epithelial cells. Mol Biol Cell. 2014;25(20):3095-104.

9. Apodaca G, Gallo LI, Bryant DM. Role of membrane traffic in the generation of epithelial cell asymmetry. Nat Cell Biol. 2012;14(12):1235-43.

10. Hegan PS, Giral H, Levi M, Mooseker MS. Myosin VI is required for maintenance of brush border structure, composition, and membrane trafficking functions in the intestinal epithelial cell. Cytoskeleton (Hoboken). 2012;69(4):235-51.

11. Vogel GF, Klee KM, Janecke AR, Muller T, Hess MW, Huber LA. Cargo-selective apical exocytosis in epithelial cells is conducted by Myo5B, Slp4a, Vamp7, and Syntaxin 3. J Cell Biol. 2015;211(3):587-604.

12. Zhang H, Kim A, Abraham N, Khan LA, Gobel V. Vesicular sorting controls the polarity of expanding membranes in the C. elegans intestine. Worm. 2013;2(1):e23702.

13. Zhang H, Kim A, Abraham N, Khan LA, Hall DH, Fleming JT, et al. Clathrin and AP-1 regulate apical polarity and lumen formation during C. elegans tubulogenesis. Development. 2012;139(11):2071-83.

14. Kang J, Shin D, Yu JR, Lee J. Lats kinase is involved in the intestinal apical membrane integrity in the nematode Caenorhabditis elegans. Development. 2009;136(16):2705-15.

15. Schneeberger K, Roth S, Nieuwenhuis EES, Middendorp S. Intestinal epithelial cell polarity defects in disease: lessons from microvillus inclusion disease. Dis Model Mech. 2018;11(2).

16. Muller T, Hess MW, Schiefermeier N, Pfaller K, Ebner HL, Heinz-Erian P, et al. MYO5B mutations cause microvillus inclusion disease and disrupt epithelial cell polarity. Nat Genet. 2008;40(10):1163-5.

17. Wiegerinck CL, Janecke AR, Schneeberger K, Vogel GF, van Haaften-Visser DY, Escher JC, et al. Loss of syntaxin 3 causes variant microvillus inclusion disease. Gastroenterology. 2014;147(1):65-8 e10.

18. Vogel GF, van Rijn JM, Krainer IM, Janecke AR, Posovszky C, Cohen M, et al. Disrupted apical exocytosis of cargo vesicles causes enteropathy in FHL5 patients with Munc18-2 mutations. JCI Insight. 2017;2(14).

19. Michaux G, Massey-Harroche D, Nicolle O, Rabant M, Brousse N, Goulet O, et al. The localisation of the apical Par/Cdc42 polarity module is specifically affected in microvillus inclusion disease. Biol Cell. 2016;108(1):19-28.

20. Knowles BC, Roland JT, Krishnan M, Tyska MJ, Lapierre LA, Dickman PS, et al. Myosin Vb uncoupling from RAB8A and RAB11A elicits microvillus inclusion disease. J Clin Invest. 2014;124(7):2947-62.

21. Dhekne HS, Pylypenko O, Overeem AW, Ferreira RJ, van der Velde KJ, Rings E, et al. MYO5B, STX3, and STXBP2 mutations reveal a common disease mechanism that unifies a subset of congenital diarrheal disorders: A mutation update. Hum Mutat. 2018;39(3):333-44.

22. McGhee JD. The C. elegans intestine. WormBook. 2007:1-36.

23. Bossinger O, Cowan CR. Methods in cell biology: analysis of cell polarity in C. elegans embryos. Methods Cell Biol. 2012;107:207-38.

24. Winter JF, Hopfner S, Korn K, Farnung BO, Bradshaw CR, Marsico G, et al. Caenorhabditis elegans screen reveals role of PAR-5 in RAB-11-recycling endosome positioning and apicobasal cell polarity. Nat Cell Biol. 2012;14(7):666-76.

25. Lee SK, Li W, Ryu SE, Rhim T, Ahnn J. Vacuolar (H+)-ATPases in Caenorhabditis elegans: what can we learn about giant H+ pumps from tiny worms? Biochim Biophys Acta. 2010;1797(10):1687-95.

26. Maxson ME, Grinstein S. The vacuolar-type H(+)-ATPase at a glance - more than a proton pump. J Cell Sci. 2014;127(Pt 23):4987-93.

27. Baars TL, Petri S, Peters C, Mayer A. Role of the V-ATPase in regulation of the vacuolar fission-fusion equilibrium. Mol Biol Cell. 2007;18(10):3873-82.

28. Hiesinger PR, Fayyazuddin A, Mehta SQ, Rosenmund T, Schulze KL, Zhai RG, et al. The v-ATPase V0 subunit a1 is required for a late step in synaptic vesicle exocytosis in Drosophila. Cell. 2005;121(4):607-20.

29. Di Giovanni J, Boudkkazi S, Mochida S, Bialowas A, Samari N, Leveque C, et al. V-ATPase membrane sector associates with synaptobrevin to modulate neurotransmitter release. Neuron. 2010;67(2):268-79.

30. Liegeois S, Benedetto A, Garnier JM, Schwab Y, Labouesse M. The V0-ATPase mediates apical secretion of exosomes containing Hedgehog-related proteins in Caenorhabditis elegans. J Cell Biol. 2006;173(6):949-61.

31. Allman E, Johnson D, Nehrke K. Loss of the apical V-ATPase a-subunit VHA-6 prevents acidification of the intestinal lumen during a rhythmic behavior in C. elegans. Am J Physiol Cell Physiol. 2009;297(5):C1071-81.

32. Knight AJ, Johnson NM, Behm CA. VHA-19 is essential in Caenorhabditis elegans oocytes for embryogenesis and is involved in trafficking in oocytes. PLoS One. 2012;7(7):e40317.

33. Zhang H, Abraham N, Khan LA, Hall DH, Fleming JT, Gobel V. Apicobasal domain identities of expanding tubular membranes depend on glycosphingolipid biosynthesis. Nat Cell Biol. 2011;13(10):1189-201.

34. Ji YJ, Choi KY, Song HO, Park BJ, Yu JR, Kagawa H, et al. VHA-8, the E subunit of V-ATPase, is essential for pH homeostasis and larval development in C. elegans. FEBS Lett. 2006;580(13):3161-6.

35. Katayama K, Kapoor K, Ohnuma S, Patel A, Swaim W, Ambudkar IS, et al. Revealing the fate of cell surface human P-glycoprotein (ABCB1): The lysosomal degradation pathway. Biochim Biophys Acta. 2015;1853(10 Pt A):2361-70.

36. Forgac M. Vacuolar ATPases: rotary proton pumps in physiology and pathophysiology. Nat Rev Mol Cell Biol. 2007;8(11):917-29.

37. Sobota JA, Back N, Eipper BA, Mains RE. Inhibitors of the V0 subunit of the vacuolar H+-ATPase prevent segregation of lysosomal- and secretory-pathway proteins. J Cell Sci. 2009;122(Pt 19):3542-53.

38. Sudhof TC, Rothman JE. Membrane fusion: grappling with SNARE and SM proteins. Science. 2009;323(5913):474-7.

39. Sato M, Saegusa K, Sato K, Hara T, Harada A, Sato K. Caenorhabditis elegans SNAP-29 is required for organellar integrity of the endomembrane system and general exocytosis in intestinal epithelial cells. Mol Biol Cell. 2011;22(14):2579-87.

40. Guo B, Liang Q, Li L, Hu Z, Wu F, Zhang P, et al. O-GlcNAc-modification of SNAP-29 regulates autophagosome maturation. Nat Cell Biol. 2014;16(12):1215-26.

41. Zhu H, Sewell AK, Han M. Intestinal apical polarity mediates regulation of TORC1 by glucosylceramide in C. elegans. Genes Dev. 2015;29(12):1218-23.

42. Collaco AM, Geibel P, Lee BS, Geibel JP, Ameen NA. Functional vacuolar ATPase (V-ATPase) proton pumps traffic to the enterocyte brush border membrane and require CFTR. Am J Physiol Cell Physiol. 2013;305(9):C981-96.

618 43. Kang J, Bai Z, Zegarek MH, Grant BD, Lee J. Essential roles of snap-29 in C. elegans.
619 Dev Biol. 2011;355(1):77-88.

620 44. Iancu TC, Mahajnah M, Manov I, Shaoul R. Microvillous inclusion disease:
621 ultrastructural variability. Ultrastruct Pathol. 2007;31(3):173-88.

622 45. Mosa MH, Nicolle O, Maschalidi S, Sepulveda FE, Bidaud-Meynard A, Menche C, et al.
623 Dynamic formation of microvillus inclusions during enterocyte differentiation in Munc18-2
624 deficient intestinal organoids. Cellular and Molecular Gastroenterology and Hepathology.
625 2018;*in press*.

626 46. Ruemmele FM, Schmitz J, Goulet O. Microvillous inclusion disease (microvillous
627 atrophy). Orphanet J Rare Dis. 2006;1:22.

628 47. Vogel GF, Hess MW, Pfaller K, Huber LA, Janecke AR, Muller T. Towards
629 understanding microvillus inclusion disease. Mol Cell Pediatr. 2016;3(1):3.

630 48. Vogel GF, Janecke AR, Krainer IM, Gutleben K, Witting B, Mitton SG, et al. Abnormal
631 Rab11-Rab8-vesicles cluster in enterocytes of patients with microvillus inclusion disease.
632 Traffic. 2017;18(7):453-64.

633 49. Talmon G, Holzapfel M, DiMaio DJ, Muirhead D. Rab11 is a useful tool for the
634 diagnosis of microvillous inclusion disease. Int J Surg Pathol. 2012;20(3):252-6.

635 50. Reinshagen K, Naim HY, Zimmer KP. Autophagocytosis of the apical membrane in
636 microvillus inclusion disease. Gut. 2002;51(4):514-21.

637 51. Marion S, Hoffmann E, Holzer D, Le Clainche C, Martin M, Sachse M, et al. Ezrin
638 promotes actin assembly at the phagosome membrane and regulates phago-lysosomal
639 fusion. Traffic. 2011;12(4):421-37.

640 52. Chang JT, Kumsta C, Hellman AB, Adams LM, Hansen M. Spatiotemporal regulation of
641 autophagy during Caenorhabditis elegans aging. Elife. 2017;6.

642 53. O'Rourke EJ, Soukas AA, Carr CE, Ruvkun G. C. elegans major fats are stored in
643 vesicles distinct from lysosome-related organelles. Cell Metab. 2009;10(5):430-5.

644 54. Wang P, Liu B, Zhang D, Belew MY, Tissenbaum HA, Cheng JX. Imaging lipid
645 metabolism in live Caenorhabditis elegans using fingerprint vibrations. Angew Chem Int Ed
646 Engl. 2014;53(44):11787-92.

647 55. Sidhaye J, Pinto CS, Dharap S, Jacob T, Bhargava S, Sonawane M. The zebrafish
648 goosepimples/myosin Vb mutant exhibits cellular attributes of human microvillus inclusion
649 disease. Mech Dev. 2016;142:62-74.

650 56. Kozik P, Hodson NA, Sahlender DA, Simecek N, Soromani C, Wu J, et al. A human
651 genome-wide screen for regulators of clathrin-coated vesicle formation reveals an
652 unexpected role for the V-ATPase. Nat Cell Biol. 2013;15(1):50-60.

653 57. Balklava Z, Pant S, Fares H, Grant BD. Genome-wide analysis identifies a general
654 requirement for polarity proteins in endocytic traffic. Nat Cell Biol. 2007;9(9):1066-73.

58. Colombie N, Choesmel-Cadamuro V, Series J, Emery G, Wang X, Ramel D. Non-autonomous role of Cdc42 in cell-cell communication during collective migration. Dev Biol. 2017;423(1):12-8.

59. Bryant DM, Datta A, Rodriguez-Fraticelli AE, Peranen J, Martin-Belmonte F, Mostov KE. A molecular network for de novo generation of the apical surface and lumen. Nat Cell Biol. 2010;12(11):1035-45.

60. Desclozeaux M, Venturato J, Wylie FG, Kay JG, Joseph SR, Le HT, et al. Active Rab11 and functional recycling endosome are required for E-cadherin trafficking and lumen formation during epithelial morphogenesis. Am J Physiol Cell Physiol. 2008;295(2):C545-56.

61. Morel N, Dedieu JC, Philippe JM. Specific sorting of the a1 isoform of the V-H+ATPase a subunit to nerve terminals where it associates with both synaptic vesicles and the presynaptic plasma membrane. J Cell Sci. 2003;116(Pt 23):4751-62.

62. Merkulova M, Paunescu TG, Azroyan A, Marshansky V, Breton S, Brown D. Mapping the H(+) (V)-ATPase interactome: identification of proteins involved in trafficking, folding, assembly and phosphorylation. Sci Rep. 2015;5:14827.

63. Steegmaier M, Yang B, Yoo JS, Huang B, Shen M, Yu S, et al. Three novel proteins of the syntaxin/SNAP-25 family. J Biol Chem. 1998;273(51):34171-9.

64. Halac U, Lacaille F, Joly F, Hugot JP, Talbotec C, Colomb V, et al. Microvillous inclusion disease: how to improve the prognosis of a severe congenital enterocyte disorder. J Pediatr Gastroenterol Nutr. 2011;52(4):460-5.

65. Feng Q, Bonder EM, Engevik AC, Zhang L, Tyska MJ, Goldenring JR, et al. Disruption of Rab8a and Rab11a causes formation of basolateral microvilli in neonatal enteropathy. J Cell Sci. 2017;130(15):2491-505.

66. Gravotta D, Carvajal-Gonzalez JM, Mattera R, Deborde S, Banfelder JR, Bonifacino JS, et al. The clathrin adaptor AP-1A mediates basolateral polarity. Dev Cell. 2012;22(4):811-23.

67. Hase K, Nakatsu F, Ohmae M, Sugihara K, Shioda N, Takahashi D, et al. AP-1B-mediated protein sorting regulates polarity and proliferation of intestinal epithelial cells in mice. Gastroenterology. 2013;145(3):625-35.

68. Simons K, Sampaio JL. Membrane organization and lipid rafts. Cold Spring Harb Perspect Biol. 2011;3(10):a004697.

69. Coskun U, Simons K. Membrane rafting: from apical sorting to phase segregation. FEBS Lett. 2010;584(9):1685-93.

70. Danielsen EM, Hansen GH. Lipid raft organization and function in brush borders of epithelial cells. Mol Membr Biol. 2006;23(1):71-9.

71. Poole K, Meder D, Simons K, Muller D. The effect of raft lipid depletion on microvilli formation in MDCK cells, visualized by atomic force microscopy. FEBS Lett. 2004;565(1-3):53-8.

72. Brenner S. The genetics of Caenorhabditis elegans. Genetics. 1974;77(1):71-94.

73. Kamath RS, Ahringer J. Genome-wide RNAi screening in Caenorhabditis elegans. Methods. 2003;30(4):313-21.

74. Kolotuev I, Bumbarger DJ, Labouesse M, Schwab Y. Targeted ultramicrotomy: a valuable tool for correlated light and electron microscopy of small model organisms. Methods Cell Biol. 2012;111:203-22.

75. Nicolle O, Burel A, Griffiths G, Michaux G, Kolotuev I. Adaptation of Cryo-Sectioning for IEM Labeling of Asymmetric Samples: A Study Using Caenorhabditis elegans. Traffic. 2015;16(8):893-905.

76. Gillard G, Shafaq-Zadah M, Nicolle O, Damaj R, Pecreaux J, Michaux G. Control of E-cadherin apical localisation and morphogenesis by a SOAP-1/AP-1/clathrin pathway in C. elegans epidermal cells. Development. 2015;142(9):1684-94.

Figure 1. V0-ATPase controls the apical localization of polarity and brush border components. (A-C) Larvae expressing endogenous ERM-1::mNG, PAR-6::GFP and GFP::PKC-3 were imaged after 72h silencing of V0-ATPase (*vha-1(RNAi))* or V1-ATPase (*vha-8(RNAi))* subunits. Arrows show the intestinal apical PM. Arrowheads show the basolateral mislocalization of markers upon *vha-1(RNAi)*. The percentage of worms displaying basolateral PAR polarity markers and the number of worms analyzed are indicated on each panel. (D-F) Quantification of the apical/cytoplasmic (Ap/cyto) ratio of ERM-1::mNG (D), PAR-6::GFP (E) and GFP::PKC-3 (F) upon 72h silencing of V0-ATPase (*vha-1*, *-4*, *-19*) or V1-ATPase (*vha-8*, *-15*) subunits (n=3-5 independent experiments). (G) V0-ATPase subunits (*vha-1*, *-4*, *-19*) knockdown specifically induces a basolateral relocalization of ERM-1. Histogram shows the basolateral/cytoplasmic (Bl/cyto) ratio of ERM-1::mNG. Dotted red line indicates a ratio of 1, which means no basolateral localization. (H-K) V0-ATPase silencing does not affect the polarity of the apical transmembrane proteins PEPT-1 and PGP-1. Strains expressing exogenously (PEPT-1) or endogenously (PGP-1)-tagged markers were silenced for *vha-1* or *vha-8* during 72h and imaged. Histograms in (J-K) represent the quantification of the Ap/cyto ratio. Arrows show the intestinal apical PM. Arrowheads show the basolateral mislocalization of markers upon *vha-1(RNAi)*. Histograms are mean ± SEM, dots represent individual worms and total number of worms from 3 independent experiments is indicated in brackets. n.s., non-significant, *p<0.05, **p<0.01, ***p<0.001, ****p<0.0001. Scale bars, 5 μm.

Figure 2. V0-ATPase affects apical trafficking via RAB-11 apical recycling endosomes.

(A-C) V-ATPase complex silencing affects the morphology of lysosomes. (A) Ultrastructural characterization of transversely-sectioned control (L4440), V0-ATPase (*vha-1*) or V1-ATPase (*vha-8*) depleted worms (72h RNAi). While lysosomes with normal morphology and size (~0.5μm) were rarely observed in control worms (left panel, arrowhead and insert), cytoplasmic enlarged "mixed organelles" with distinct lysosomal and vesicular regions were observed upon both *vha-1* and *vha-8(RNAi)* (arrows). (B) Quantification of the number of mixed organelles (n=1-5grid/larvae, n=7-13 larvae). (C) shows the accumulation of the lysosomal marker LMP-1::GFP in large cytoplasmic structures (arrowheads) upon both *vha-1* and *vha-8(RNAi)*. (D) Ultrastructural characterization of transversely-sectioned control (L4440), V0-ATPase (*vha-1*) and V1-ATPase (*vha-8*) depleted worms. Middle panel shows the specific accumulation of cytoplasmic electron-lucent vesicles upon *vha-1(RNAi)*. (E-H) V0- or V1-ATPase silencing marginally decreases the number of RAB-5^{+} vesicles but V0-ATPase knockdown specifically disrupts RAB-11^{+} apical recycling endosomes. Confocal imaging of the endosomal markers of apical early/sorting (RAB-5, E) and apical recycling (RAB-11, G) endosomes in control, *vha-1(RNAi)* and *vha-8(RNAi)* conditions. (F-H) Quantification of the number of RAB-5+ vesicles (F) and RAB-11 apical/cytoplasmic (Ap/cyto) ratio (H) (n=3). (I-J) *rab-11(RNAi)* phenocopies V0-ATPase depletion on ERM-1::GFP polarity. ERM-1::GFP expressing worms were silenced for *rab-11* during 72h and imaged. Arrowheads show the basolateral accumulation of ERM-1. (J) shows ERM-1 basolateral/cytoplasmic (Bl/cyto) ratio quantification (n=3). Histograms are mean ± SEM on each panel, dots represent individual worms and the total number of worms from 3 independent experiments is indicated in brackets. L, lumen; mv, microvilli; Ly, lysosome. n.s., non-significant, *p<0.05, ***p<0.001, ****p<0.0001. Scale bars, 5 μm.

Figure 3. SNAP-29 acts downstream of V0-ATPase in polarity maintenance.
(A-C) V0-ATPase silencing specifically decreases the apical localization of SNAP-29::GFP. Strains expressing the indicated markers were silenced for V0- (*vha-1*) or V1-(*vha-8*) ATPase during 72h and imaged. Histograms represent the quantification of the apical/cytoplasmic (Ap/cyto) ratio of each marker. (D-E) *snap-29(RNAi)* induces a basolateral localization of ERM-1. *snap-29* was knocked down by RNAi in ERM-1::GFP-expressing strains and its localization was recorded after 72h. (E) represents the quantification of the basolateral/cytoplasmic (Bl/cyto) ratio of ERM-1::GFP. Arrows and arrowheads indicate the apical and basolateral PM, respectively. (F) Super-resolution imaging of the apical PM. Strains expressing the indicated markers were mounted and imaged. * indicate endogenously-tagged markers, arrowheads and arrows indicate microvilli and presumptive terminal web, respectively. Scale bars, 5 μm (A-D) and 2 μm (F). Histograms are mean ± SEM on each panel, dots represent individual worms and the total number of worms from 3 independent experiments is indicated in brackets. n.s., non-significant, *$p<0.05$, **$p<0.01$, ****$p<0.0001$.

Fig 4. V0-ATPase depletion induces a microvillus atrophy in *C. elegans*

(A) Precise visualization of microvilli by super-resolution (upper panels, 96h RNAi, ERM-1::GFP) and TEM (lower panels, 72h RNAi) analysis. Control animals showed the typical intestinal brush border morphology consisting of a dense brush border of microvilli surrounded by a glycocalyx and stabilized by the terminal web, a network of actin and intermediate filaments running below and in parallel to the apical plasma membrane. Conversely, *vha-1(RNAi)* worms display a microvillus atrophy, with irregular, shorter and sparse microvilli, a phenotype that is not observed in *vha-8* depleted worms. The terminal web appears normal in all cases. L, lumen; mv, microvilli; tw, terminal web. (B-C) Measurement of microvilli length (B) and width (C) upon 72h V0 and V1-ATPase knockdown from TEM images. Data are mean ± SEM, n=5 microvilli/worm on the number of worms indicated in brackets. n.s., non-significant, ***p<0,001, ****p<0.0001. (D) The brush border components ACT-5 and ERM-1 localize to the basolateral PM with a microvilli-like pattern upon 96h *vha-1(RNAi)*. Lower panels are magnified images of the selected areas.

Fig 5. V0-ATPase silencing induces MVID in *C. elegans*

(A-B) 96h V0-ATPase knockdown (*vha-1(RNAi)*) induces the formation of cytoplasmic ERM-1^+ and ACT-5^+ microvillus inclusion-like structures. (C) Line scan shows that rounded structures found in the cytoplasm (lower panel) display similar periodic pattern than that of apical microvilli (upper panel). A line scan of 4 μm was performed (dotted line) on ERM-1::mNG expressing worms apical PM (control worms) and on ERM-1::mNG$^+$ MVI-like structures (96h of *vha-1(RNAi)*). (D-E) GFP::PKC-3 and SNAP-29::GFP localize to *vha-1(RNAi)* induced MVI-like structures. Insert is a magnified image of the structure indicated by the arrowhead. (F-H) V0-ATPase silencing mostly induces cytoplasmic ERM-1^+ vacuoles/irregular MVIs as well as typical MVIs. (F-G) Ultrastructural analysis of cytoplasmic inclusions observed in *C. elegans* silenced for *vha-1* during 96h by TEM. Note the classical MVIs showing the symmetrical, mainly inward-pointing arrangement of microvilli (arrowheads) and the area around the inclusion corresponding to the terminal web (arrows). Typical MVIs were found in 3/16 worms. (G) Numerous and larger 'irregular' vacuole-inclusions with a wide heterogeneity in size, shape, and electron-density were found upon 96h *vha-1* silencing. The lumen contains probably amorphous, microvesicular, membranous and lipid components. (H) Immuno-EM analysis of vacuole-like structures using phospho-ezrin antibody and nanogold protein A gold in *vha-1(RNAi)* worms (96h) (dark dots). Anti-phospho-ezrin antibody accumulates around *vha-1(RNAi)*-induced vacuole-like structures and on the apical PM. (I) *snap-29(RNAi)* (96h) also induced the formation of cytoplasmic ERM-1::mNG$^+$ MVIs. Lower panel is a magnified picture of the MVI indicated by the arrowhead. L, lumen; mv, microvilli; tw, terminal web; AP, apical PM; BS, basal PM. ****$p<0.0001$.

Fig 6. Dynamics of microvillus inclusions in *C. elegans*

(A) MVIs cytoplasmic nucleation observed by timelapse imaging in endogenous ERM-1::mNG expressing worms silenced for *vha-1* during 96h. Figure shows snapshots every 5 min, MVI is indicated by the arrow. (B) MVIs can arise by internalization of the apical or basolateral PM. ERM-1::GFP expressing worms were silenced for *vha-1* during 72h and imaged by conventional (left panel) or super-resolution (right panel) microscopy. Arrowhead and arrow show the apical and basolateral PM, respectively. (C) Irregular MVIs/vacuoles (arrow) are often in the vicinity of lysosomes/mixed-organelles (arrowhead). N2 worms were silenced for *vha-1* during 96h and analyzed by TEM. (D) ERM-1::wSc and LMP-1::GFP colocalize at *vha-1(RNAi)*-induced MVIs (96h). (E-F) 96h *vha-1(RNAi)*-induced MVIs are often surrounded by a second ERM-1^{+} layer in which MVIs are degraded. (E) shows a super-resolution image of an MVI (arrowhead) and the surrounding ERM-1^{+} layer (arrow), (F) shows a timelapse imaging of *vha-1(RNAi)*-induced MVI disappearance (image every 4 min). (G-H) Autophagy is activated more upon *vha-1(RNAi)* than *vha-8(RNAi)*. LGG-1::GFP expressing worms were silenced for *vha-1* or *vha-8* during 72h and imaged. (H) shows the quantification of LGG-1::GFP apical/cytoplasmic (Ap/cyto) ratio. Histograms are mean ± SEM on each panel, dots represent individual worms and the total number of worms from 3 independent experiments is indicated in brackets.

Fig 7. V0-ATPase depletion defects can be counteracted by cholesterol supplementation. (A-B) Cholesterol supplementation partially rescues V0-ATPase depletion-induced structural and polarity defects. ERM-1::mNG expressing worms were silenced for *vha-1* and cultured on normal (5 ug.ml-1) or high (50 ug.ml-1) concentration of cholesterol in NGM medium. (A) Cholesterol supplementation partly corrects the microvillus atrophy induced by V0-ATPase depletion. ERM-1::mNG expressing worms were silenced for *vha-1* during 96h, imaged and the length of the microvilli was measured as described in methods (n=4 independent experiments). (B) Cholesterol decreases the basolateral mislocalization induced by *vha-1(RNAi)*. ERM-1::GFP expressing worms were silenced for *vha-1* during 72h, imaged and the basolateral/cytoplasmic ratio of ERM-1 was quantified (n=5 independent experiments). Histograms are mean ± SEM on each panel, dots represent individual worms and the number of worms used is indicated in brackets. *p<0,05, ***p<0,001.

Supporting information

S1 Fig. V0-ATPase silencing affects the polarized localization of polarity modules and brush border components. (A) Polarity screen results. GFP::CDC-42 (upper panels) and ERM-1::GFP (lower panels) expressing strains were silenced for control (L4440), V0-ATPase (*vha-1*) or V1-ATPase (*vha-8*) specific RNAi during 72h and imaged. Note the basolateral accumulation of both markers upon *vha-1(RNAi)*. (B-C) Effect of 72h *vha-1(RNAi)* on the expression of the V0-ATPase subunit VHA-6::mCh. (B) shows representative images and (C) the quantification of VHA-6::mCh apical/cytoplasmic ratio. The histogram shows the mean ± SEM, dots represent individual worms and the total number of worms from 3 independent experiments is indicated in brackets. ****p<0.0001. (C) 72h *vha-6(RNAi)* also induces a basolateral mislocalization of ERM-1::GFP (arrowheads). Arrows and arrowheads show the apical and basolateral PM, respectively.

S2 Fig. V0-ATPase polarity maintenance pathway. (A-B) Effect of 72h V0- or V1-ATPase silencing on the basolateral/cytoplasmic (Bl/cyto) ratio of SLCF-1. (B) Both *vha-1* and *vha-8(RNAi)* (72h) induce an accumulation of GFP::RAB-7 and GFP::RAB-10 in large cytoplasmic structures. (C) Effect of 72h V0- or V1-ATPase silencing on the basolateral/cytoplasmic (Bl/cyto) ratio of SYX-1/SYN-1. (D-F) *snap-29(RNAi)* decreases SNAP-29::GFP expression and CDC-42::GFP apical localization. (E) represents the apical/cytoplasmic ratio of SNAP-29::GFP. (G-H) *rab-11(RNAi)* decreases RAB-11 expression. (H) shows the quantification of RAB-11::GFP apical/cytoplasmic ratio. Histograms are mean ± SEM on each panel, dots represent individual worms and the total number of worms from 3 (A, C) or 1 (E, F) experiment(s) is indicated in brackets. n.s. non-significant, ***p<0,001, ****p<0,0001.

S3 Fig. Ultrastructural analysis of V0-ATPase depletion associated defects. (A) V0- or V1-ATPase subunits silencing affects *C. elegans* development. Histogram shows the measurement of the worms' diameter from TEM images. (B) *vha-1* silencing often induced a detachment of the PM from the terminal web as well as (C-D) increased the length of cell junctions (CeAJ). (D) shows the measurement of the electron-dense cell-cell junction length on TEM pictures. (E) *vha-1* depleted worms accumulate cell and/or bacterial debris in the intestinal lumen. (F) *vha-1* depleted N2 worms, contrary to control or *vha-8*-depleted worms, are devoid of yolk storage granules (arrows). L, lumen; mv, microvilli; tw, terminal web; AP, apical PM; BS, basal PM; CeAJ, *C. elegans* adherens junctions. Histograms show the mean ± SEM, dots represent individual worms and the total number of worms is indicated in brackets. n.s. non-significant, ****p<0,0001.

S4 Fig. MVIs onset by internalization of the apical PM. 3D projection of ERM-1::GFP expressing worms silenced for *vha-1* during 72h. The arrow indicates the internalization of the apical PM. Note the large hole induced by the PM invagination (arrowhead). Scale bar: 5 μm.

S5 Fig. Comparison of polarity maintenance pathways. In control cells, AP-1, Clathrin and GSLs ensure the correct sorting of polarity and brush border proteins, directly or through adaptor proteins, to the apical PM. Their PM targeting likely involves RAB-11^{+} apical recycling endosomes, from which polarity/brush border/adaptors-containing vesicles fuse with

the PM in a V0-ATPase/Myo5B/STX3/Munc18-2-dependent manner. Upon AP-1 and/or Clathrin and/or GSLs depletion, the early apical sorting step is defective, leading to a polarity inversion that induces the lateral accumulation of apical factors and the formation of lateral ectopic membranes. Upon V0-ATPase or Myo5B/STX3/Munc18-2 depletion, a late apical exocytosis step is defective, which affects only trafficking (i.e. SNAP-29 or STX3) and induces the misrouting of polarity/brush border components to the basolateral PM or in MVIs.

S1 Table. Polarity maintenance screen results. White and blue cases indicate the genes that affect CDC-42 only or CDC-42 and ERM-1 apical localization, respectively.

S2 Table. Comparison of *vha-1* and *vha-8* silencing phenotypes.

S3 Table. Comparison of MVID and V0-ATPase depletion phenotypes. Adapted from (49), with minor modifications.

S4 Table. *C. elegans* strains used in this study.

S1 Movie. Cytoplasmic nucleation of MVIs. Maximum projection of ERM-1::mNG expressing worms silenced for *vha-1* during 96h. Arrows indicate nucleating MVIs.

S2 Movie. Cytoplasmic nucleation of MVIs. Maximum projection of ERM-1::mNG expressing worms silenced for *vha-1* during 96h. Arrowheads and arrows indicate irregular MVIs/vacuoles and cytoplasmic nucleating MVIs, respectively.

S3 Movie. MVI formation by internalization of the apical PM. 3D projection of ERM-1::GFP expressing worms silenced for *vha-1* during 72h.

S4 Movie. MVI elimination. Maximum projection of ERM-1::mNG expressing worms silenced for *vha-1* during 96h. The arrow indicates the elimination of the MVIs inside the presumptive autophagic ERM-1^{+} membrane. Arrowheads show direct MVI disappearance in the cytoplasm.

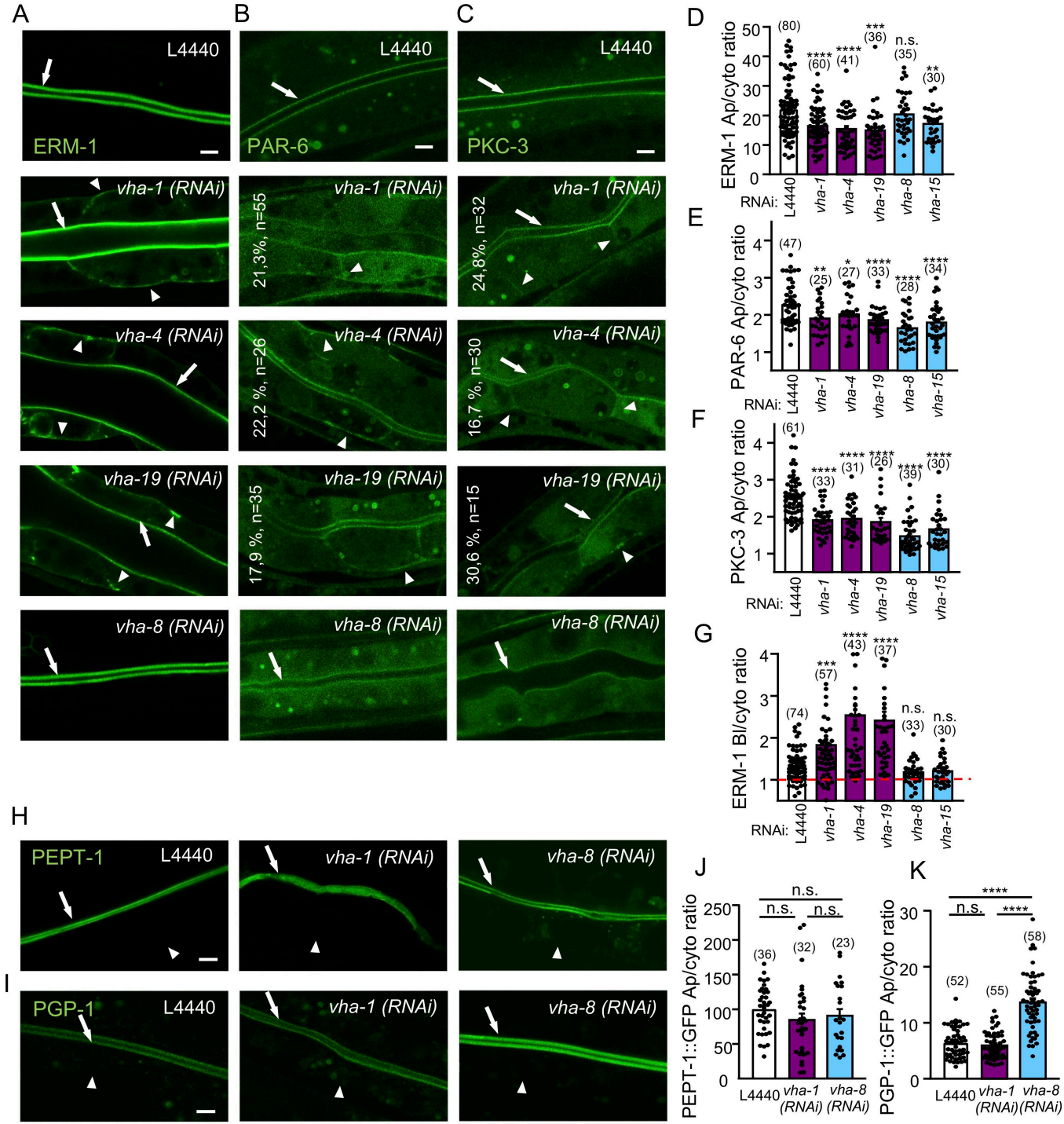
A
B
C
L4440
ERM-1
PAR-6
PKC-3
vha-1 (RNAi)
21,3%, n=55
24,8%, n=32
vha-4 (RNAi)
22,2 %, n=26
16,7 %, n=30
vha-19 (RNAi)
17,9 %, n=35
30,6 %, n=15
vha-8 (RNAi)
D
ERM-1 Ap/cyto ratio
E
PAR-6 Ap/cyto ratio
F
PKC-3 Ap/cyto ratio
G
ERM-1 BI/cyto ratio
RNAi:
L4440
vha-1
vha-4
vha-19
vha-8
vha-15
n.s.
H
PEPT-1
I
PGP-1
J
PEPT-1::GFP Ap/cyto ratio
K
PGP-1::GFP Ap/cyto ratio

Figure 1

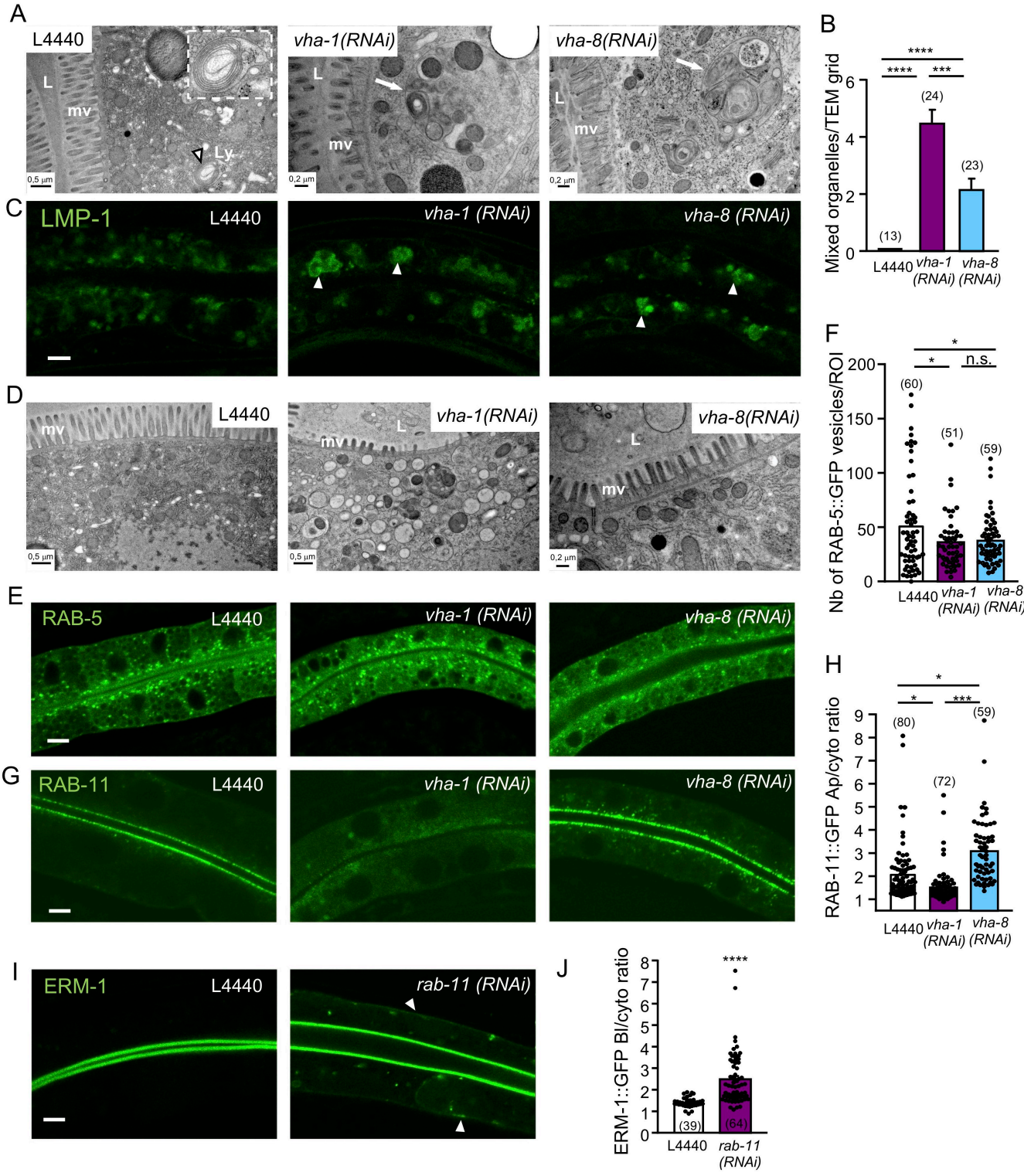
A
L4440
vha-1(RNAi)
vha-8(RNAi)
L
mv
Ly
0,5 µm
0,2 µm
B
Mixed organelles/TEM grid
****
***
(13)
(24)
(23)
L4440
vha-1 (RNAi)
vha-8 (RNAi)
C
LMP-1
L4440
vha-1 (RNAi)
vha-8 (RNAi)
D
L4440
vha-1(RNAi)
vha-8(RNAi)
E
RAB-5
L4440
vha-1 (RNAi)
vha-8 (RNAi)
F
Nb of RAB-5::GFP vesicles/ROI
*
n.s.
(60)
(51)
(59)
L4440
vha-1 (RNAi)
vha-8 (RNAi)
G
RAB-11
L4440
vha-1 (RNAi)
vha-8 (RNAi)
H
RAB-11::GFP Ap/cyto ratio
*
***
(80)
(72)
(59)
L4440
vha-1 (RNAi)
vha-8 (RNAi)
I
ERM-1
L4440
rab-11 (RNAi)
J
ERM-1::GFP Bl/cyto ratio
****
(39)
(64)
L4440
rab-11 (RNAi)

Figure 2

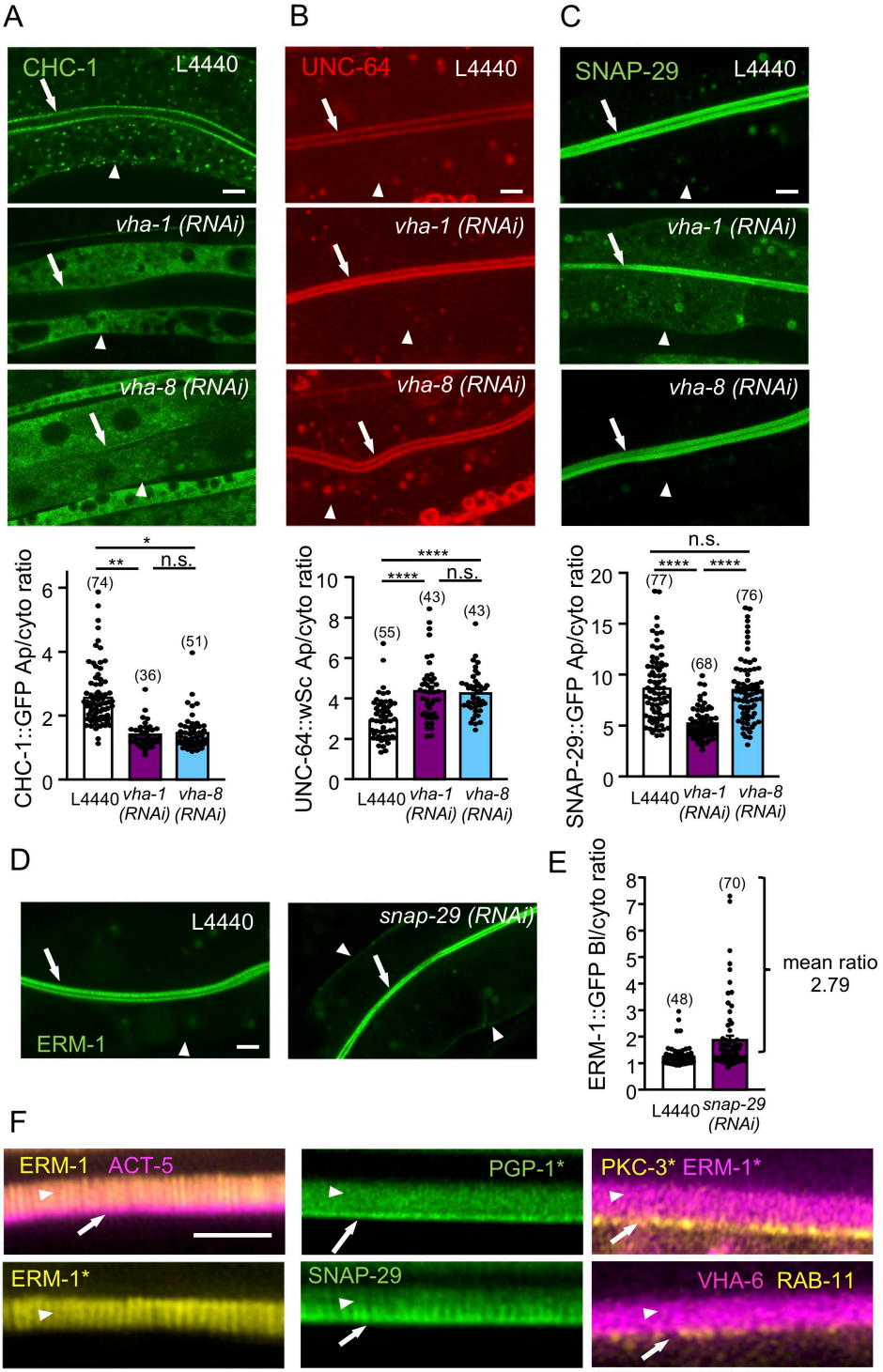
A
CHC-1
L4440
vha-1 (RNAi)
vha-8 (RNAi)
B
UNC-64
L4440
vha-1 (RNAi)
vha-8 (RNAi)
C
SNAP-29
L4440
vha-1 (RNAi)
vha-8 (RNAi)
CHC-1::GFP Ap/cyto ratio
UNC-64::wSc Ap/cyto ratio
SNAP-29::GFP Ap/cyto ratio
L4440
vha-1 (RNAi)
vha-8 (RNAi)
n.s.
D
L4440
ERM-1
snap-29 (RNAi)
E
ERM-1::GFP Bl/cyto ratio
mean ratio 2.79
L4440
snap-29 (RNAi)
F
ERM-1 ACT-5
PGP-1*
PKC-3* ERM-1*
ERM-1*
SNAP-29
VHA-6 RAB-11

Figure 3

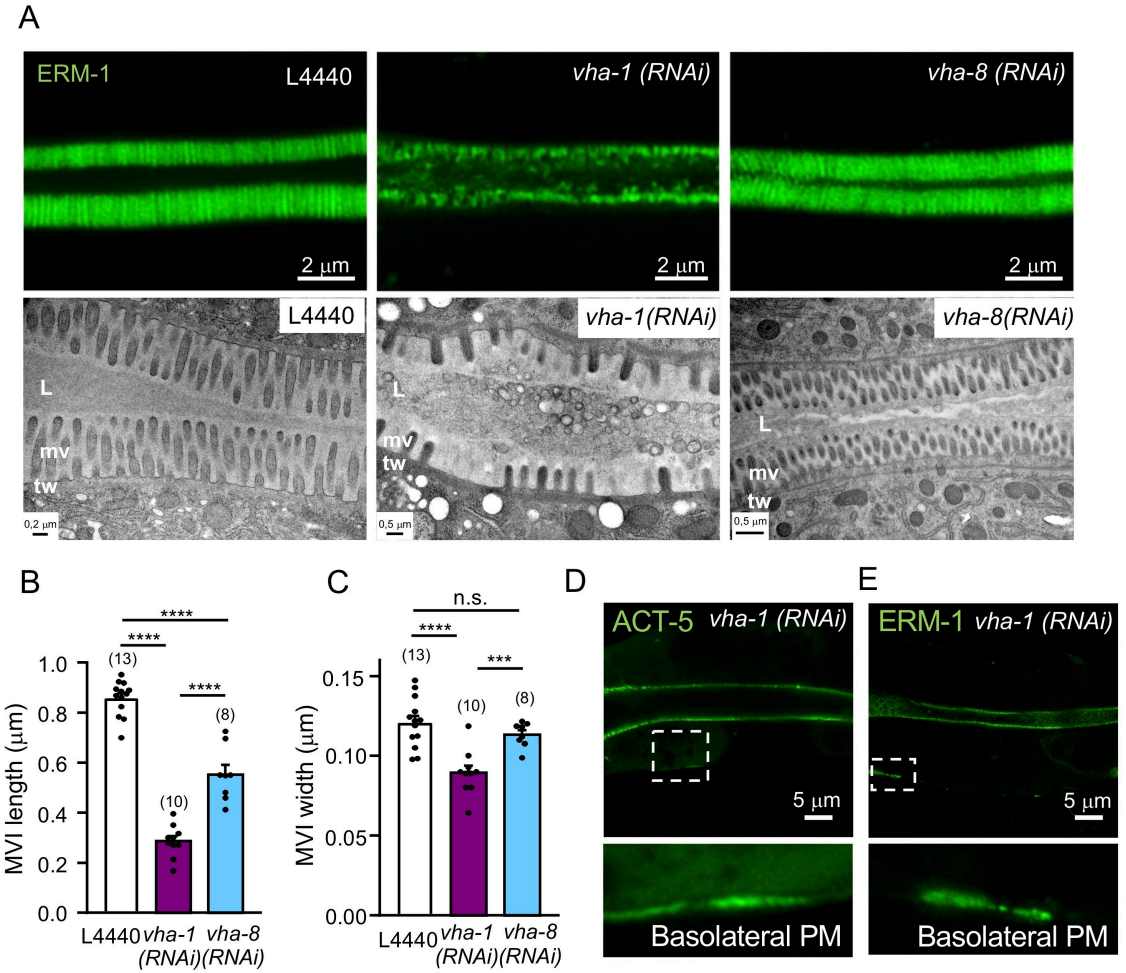
A
ERM-1
L4440
vha-1 (RNAi)
vha-8 (RNAi)
2 µm
L
mv
tw
0,2 µm
0,5 µm
B
MVI length (µm)
1.0
0.8
0.6
0.4
0.2
0.0
(13)
(10)
(8)
****
L4440
vha-1 (RNAi)
vha-8 (RNAi)
C
MVI width (µm)
0.15
0.10
0.05
0.00
n.s.
***
D
ACT-5
Basolateral PM
5 µm
E
ERM-1

Figure 4

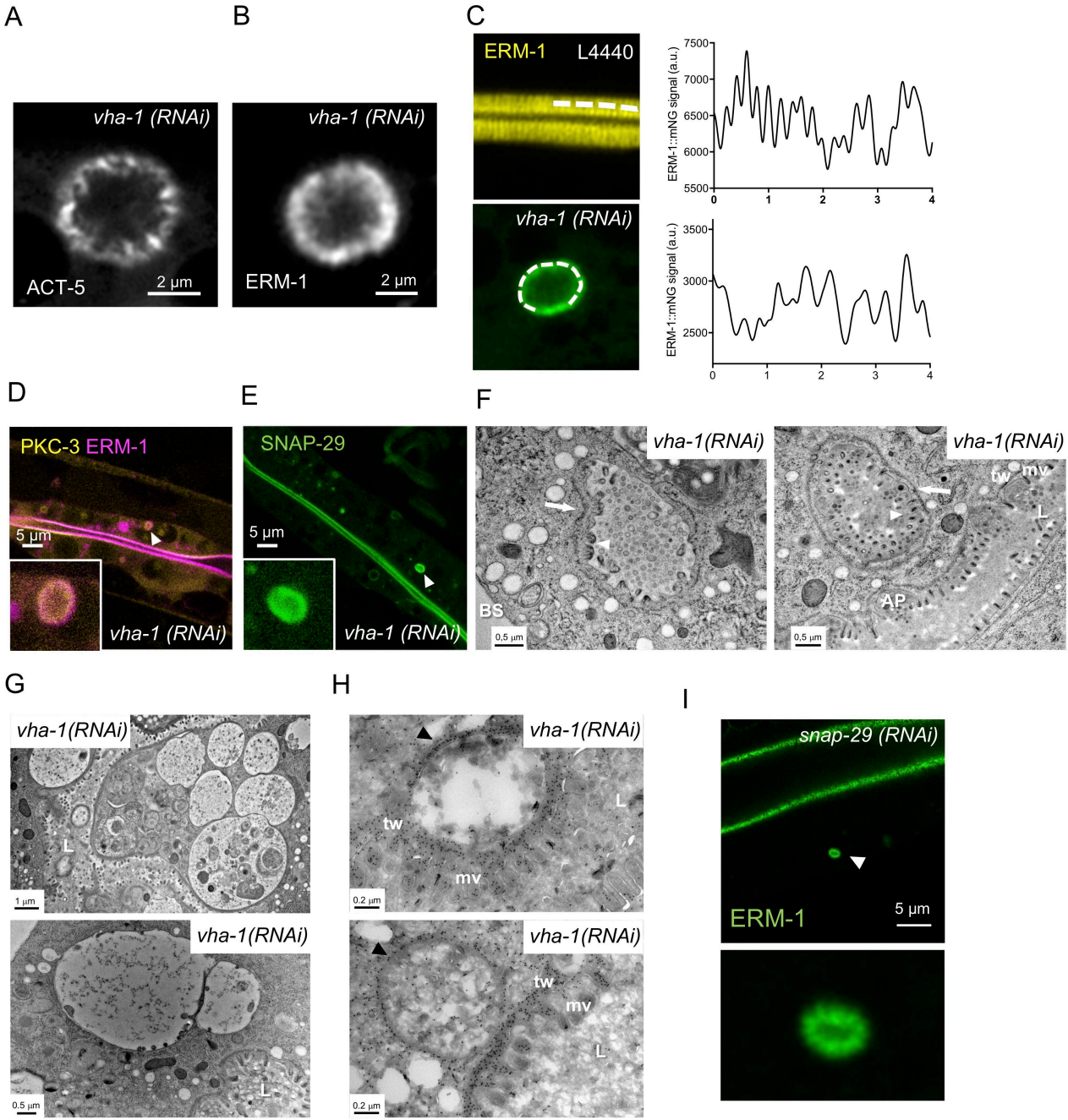
A
vha-1 (RNAi)
ACT-5
2 µm
B
vha-1 (RNAi)
ERM-1
2 µm
C
ERM-1
L4440
vha-1 (RNAi)
ERM-1::mNG signal (a.u.)
7500
7000
6500
6000
5500
0
1
2
3
4
ERM-1::mNG signal (a.u.)
3500
3000
2500
D
PKC-3 ERM-1
5 µm
vha-1 (RNAi)
E
SNAP-29
5 µm
vha-1 (RNAi)
F
vha-1(RNAi)
BS
0,5 µm
vha-1(RNAi)
tw
mv
L
AP
0,5 µm
G
vha-1(RNAi)
L
1 µm
vha-1(RNAi)
L
0,5 µm
H
vha-1(RNAi)
tw
mv
L
0.2 µm
vha-1(RNAi)
tw
mv
L
0.2 µm
I
snap-29 (RNAi)
ERM-1
5 µm

Figure 5

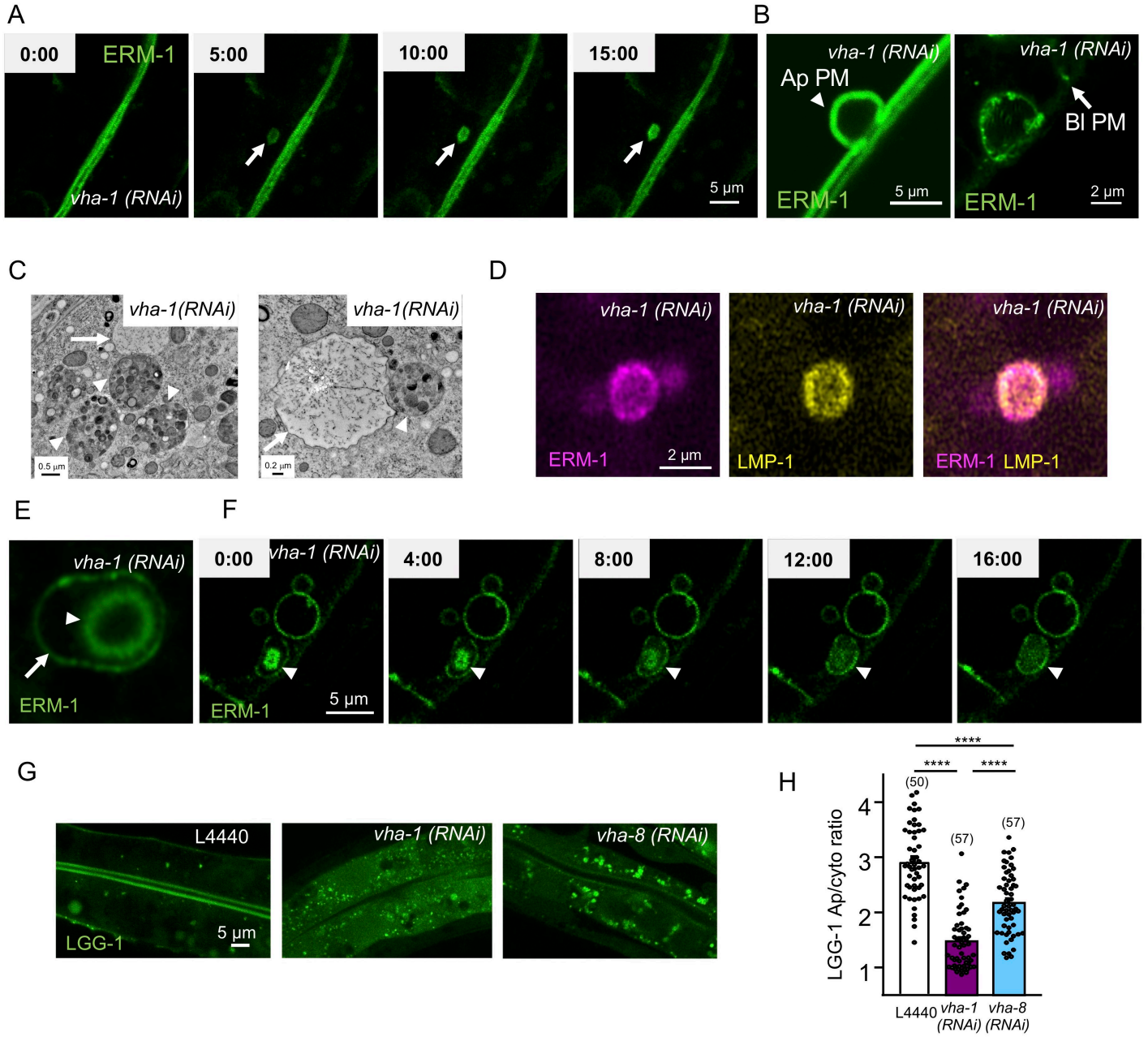
A
0:00
ERM-1
vha-1 (RNAi)
5:00
10:00
15:00
5 µm
B
vha-1 (RNAi)
Ap PM
ERM-1
5 µm
vha-1 (RNAi)
Bl PM
ERM-1
2 µm
C
vha-1(RNAi)
0.5 µm
vha-1(RNAi)
0.2 µm
D
vha-1 (RNAi)
ERM-1
2 µm
vha-1 (RNAi)
LMP-1
vha-1 (RNAi)
ERM-1 LMP-1
E
vha-1 (RNAi)
ERM-1
F
0:00
vha-1 (RNAi)
ERM-1
5 µm
4:00
8:00
12:00
16:00
G
L4440
LGG-1
5 µm
vha-1 (RNAi)
vha-8 (RNAi)
H
****
****
****
(50)
(57)
(57)
LGG-1 Ap/cyto ratio
4
3
2
1
L4440
vha-1 (RNAi)
vha-8 (RNAi)

Figure 6

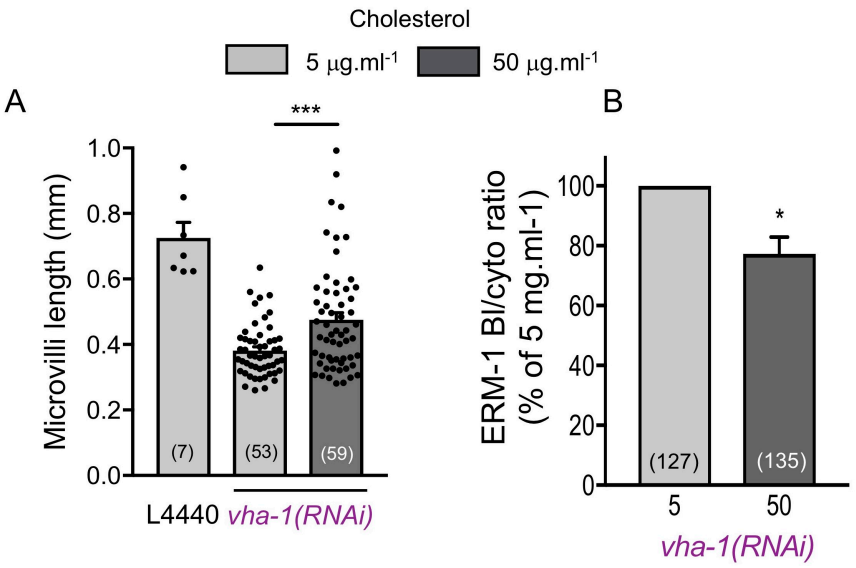
Cholesterol
5 µg.ml-1
50 µg.ml-1
A
***
Microvilli length (mm)
1.0
0.8
0.6
0.4
0.2
0.0
(7)
(53)
(59)
L4440
vha-1(RNAi)
B
ERM-1 Bl/cyto ratio
(% of 5 mg.ml-1)
100
80
60
40
20
0
*
(127)
(135)
5
50
vha-1(RNAi)

Figure 7

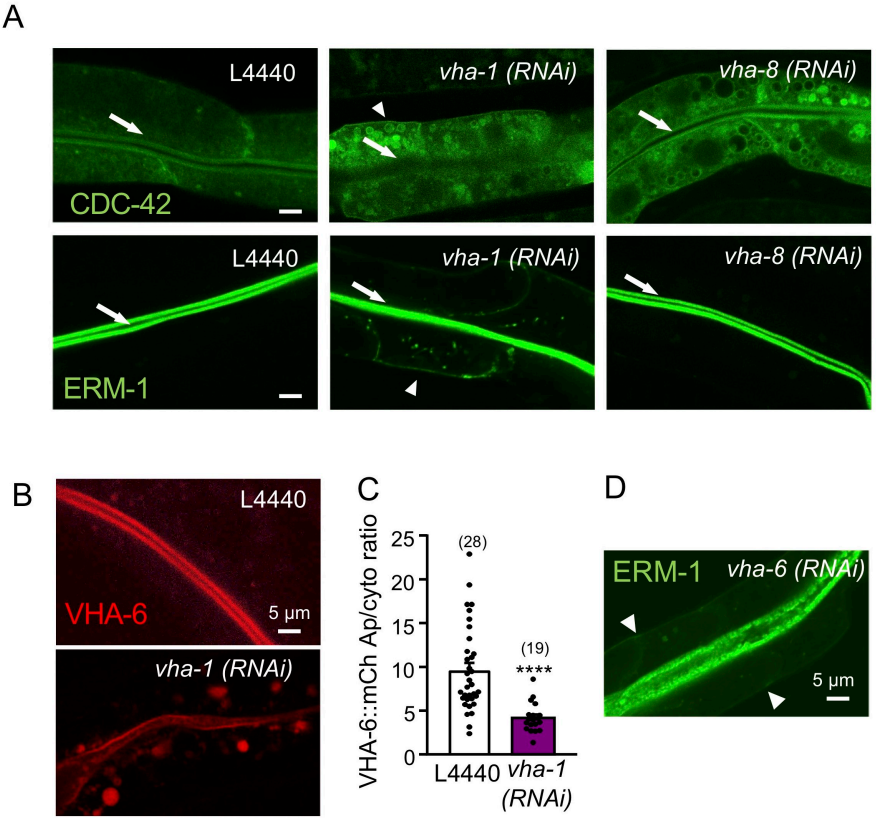
A
L4440
vha-1 (RNAi)
vha-8 (RNAi)
CDC-42
L4440
vha-1 (RNAi)
vha-8 (RNAi)
ERM-1
B
L4440
VHA-6
5 µm
vha-1 (RNAi)
C
VHA-6::mCh Ap/cyto ratio
25
20
15
10
5
0
(28)
(19)
****
L4440
vha-1 (RNAi)
D
ERM-1
vha-6 (RNAi)
5 µm

Figure S1

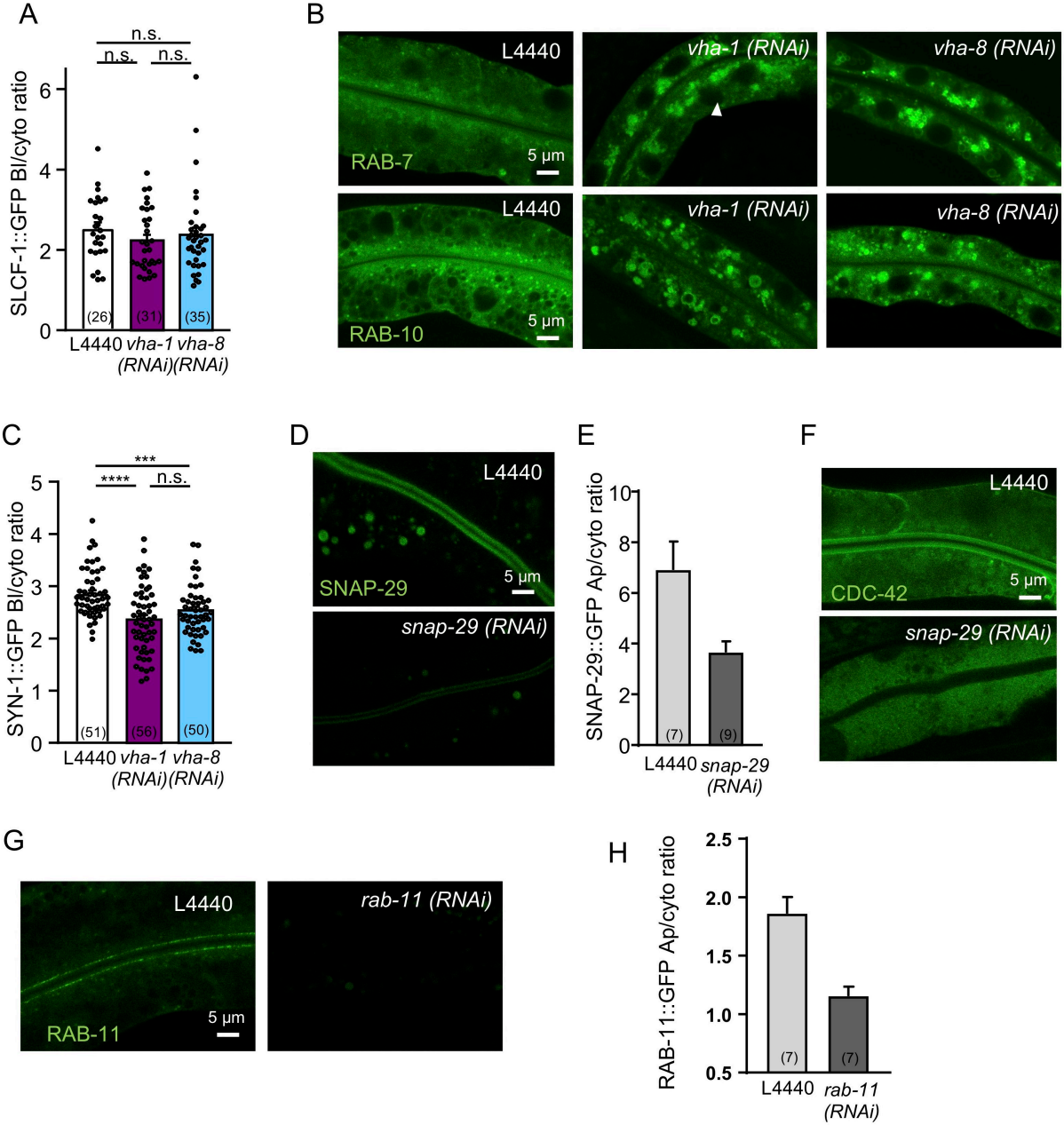
A
n.s.
n.s.
n.s.
SLCF-1::GFP Bl/cyto ratio
0
2
4
6
(26)
(31)
(35)
L4440
vha-1 (RNAi)
vha-8 (RNAi)
B
L4440
RAB-7
5 µm
vha-1 (RNAi)
vha-8 (RNAi)
L4440
RAB-10
5 µm
vha-1 (RNAi)
vha-8 (RNAi)
C
***
****
n.s.
SYN-1::GFP Bl/cyto ratio
0
1
2
3
4
5
(51)
(56)
(50)
L4440
vha-1 (RNAi)
vha-8 (RNAi)
D
L4440
SNAP-29
5 µm
snap-29 (RNAi)
E
SNAP-29::GFP Ap/cyto ratio
0
2
4
6
8
10
(7)
(9)
L4440
snap-29 (RNAi)
F
L4440
CDC-42
5 µm
snap-29 (RNAi)
G
L4440
RAB-11
5 µm
rab-11 (RNAi)
H
RAB-11::GFP Ap/cyto ratio
0.5
1.0
1.5
2.0
2.5
(7)
(7)
L4440
rab-11 (RNAi)

Figure S2

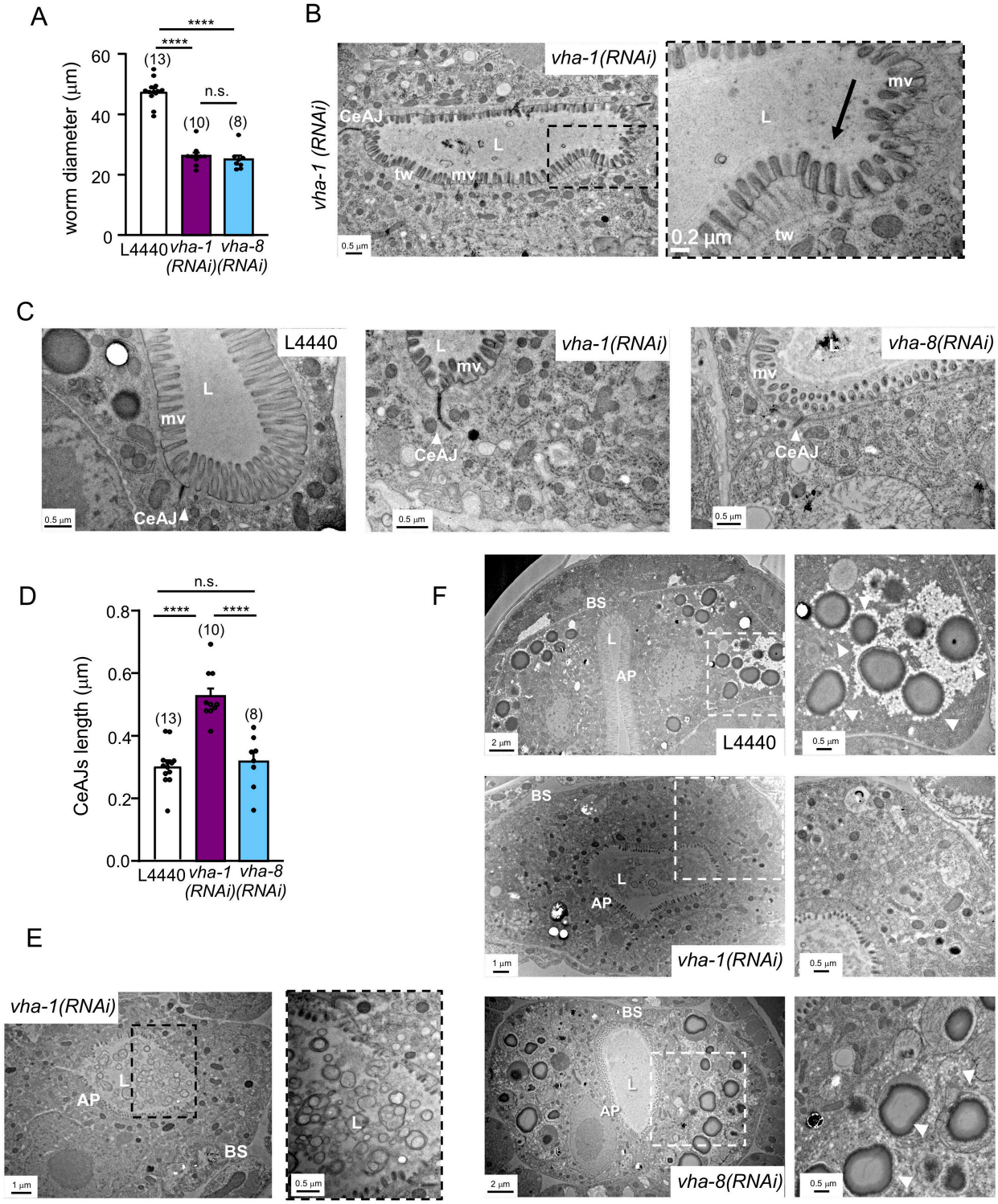
A
****
****
n.s.
(13)
(10)
(8)
worm diameter (μm)
60
40
20
0
L4440
vha-1 (RNAi)
vha-8 (RNAi)
B
vha-1 (RNAi)
vha-1(RNAi)
CeAJ
L
tw
mv
0.5 μm
0.2 μm
C
L4440
vha-1(RNAi)
vha-8(RNAi)
L
mv
CeAJ
0.5 μm
D
n.s.
****
****
(13)
(10)
(8)
CeAJs length (μm)
0.8
0.6
0.4
0.2
0.0
L4440
vha-1 (RNAi)
vha-8 (RNAi)
E
vha-1(RNAi)
AP
L
BS
1 μm
0.5 μm
F
BS
L
AP
L4440
vha-1(RNAi)
vha-8(RNAi)
2 μm
1 μm
0.5 μm

Figure S3

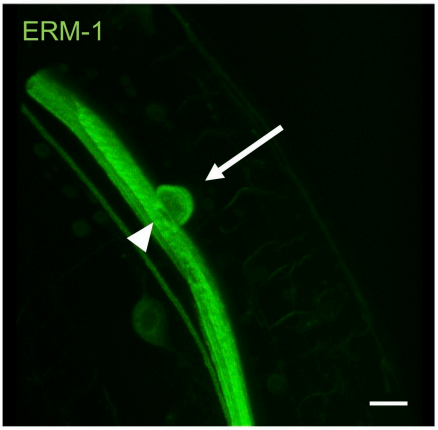

Figure S4

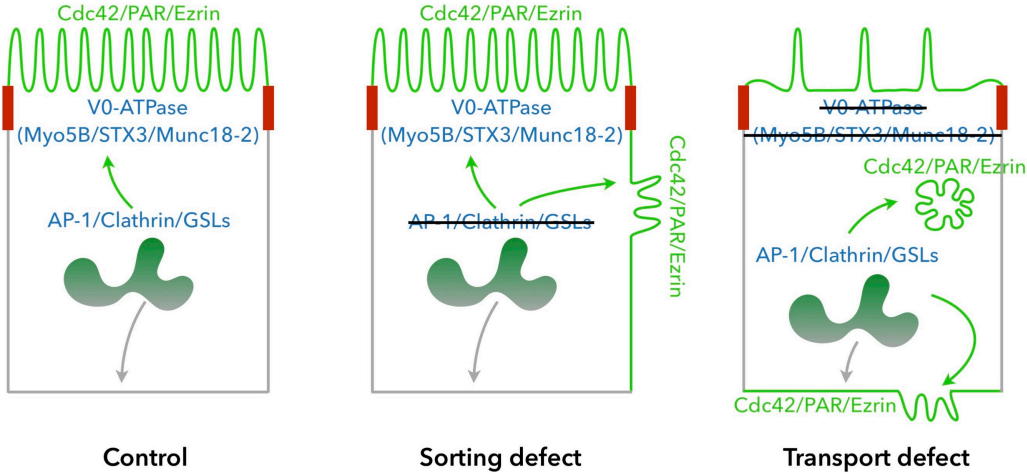
Cdc42/PAR/Ezrin
V0-ATPase
(Myo5B/STX3/Munc18-2)
AP-1/Clathrin/GSLs
Control
Cdc42/PAR/Ezrin
V0-ATPase
(Myo5B/STX3/Munc18-2)
AP-1/Clathrin/GSLs
Cdc42/PAR/Ezrin
Sorting defect
V0-ATPase
(Myo5B/STX3/Munc18-2)
Cdc42/PAR/Ezrin
AP-1/Clathrin/GSLs
Cdc42/PAR/Ezrin
Transport defect

Figure S5

S1 Table: Polarity maintenance screen results

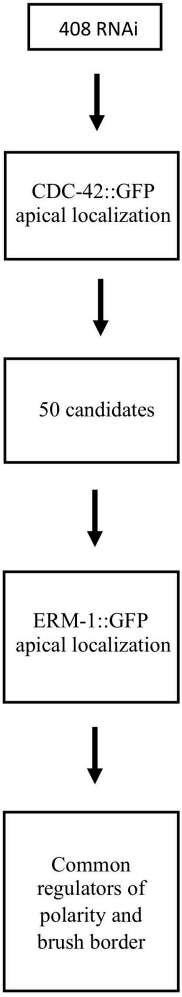

Family	Gene
COPI	E03H4.8
	copb-1
	COPI zeta
	copb-2
Cytoskeleton	act-5
	IFB-1
ECM	noah-1
ER traffic	lpin-1
	sly-1
ESCRTIII	vps-32.1
F ATPase	H28O16.2
GSL	fasn-1
	pod-2
	sptl-1
Membrane fusion	nsf-1
	snap-29
	snap-1
	unc-64
	syx-3
	syx-5
	syx-7
Muscle	let-805
	vab-10
	pat-10
NADPH oxidase	bli-3
Sorting	aps-1
	chc-1
PAR	cdc-42
Rabs	rab-5
Ribosome	rpl-36
V-ATPase	vha-4
	unc-32
	vha-1
	vha-19
	vha-17
	vha-15
	vha-20
	vha-10
	vha-8
	vha-12

S2 Table : Comparison of *vha-1* and *vha-8* silencing phenotypes

	L4440	***vha-1(RNAi) (V0)***	***vha-8(RNAi) (V1)***
PAR-6, PKC-3, ERM-1 apical PM	Normal	Down	Down
Basolateral PAR-6, PKC-3, ERM-1	No	Yes	No
SNAP-29 cytoplasmic accumulation	No	Yes	No
Mixed organelles	No	Yes	Yes
LMP-1, RAB-7, RAB-10 accumulation	No	Yes	Yes
Autophagy activation	No	+++	+
Accumulation of cytoplasmic lucent vesicles	No	Yes	No
RAB-11 signal	-	Down	Up
Microvillus atrophy	No	Yes	No
MVIs, vacuoles	No	Yes	No

S3 Table: Comparison of MVID and V0-ATPase depletion phenotypes.
Adapted from (49), with minor modifications.

MVID phenotype	Normal intestine	*MYO5B* deficient patients	*STX3* deficient patients	*MUNC18-2* deficient patients (FHL5)	*MUNC18-2* -/- mouse organoids	*vha-1* RNAi *C. elegans*
microvillus atrophy (absent or abnormal microvilli)	no	yes	yes	yes	yes	yes (Fig 4)
microvillus inclusions	no	frequent, observed in 10% of cells	infrequent	infrequent, not fully penetrant	frequent but only after differentiation	infrequent (Fig 5)
basolateral microvilli	no	incomplete penetrance	frequent	frequent	frequent but only after differentiation	probable (Fig 5)
vesicle or tubulo-vesicular structures accumulation	no	Apical vesicles and tubulovesicular; variable electron-dense and translucent	Apical vesicles and tubulovesicular; variable electron-dense and translucent (villus)	electron-dense and translucent apical vesicles	crypt: translucent apical villus: translucent tubulovesicular apical	endosome like vesicles and enlarged vacuolar structures (Fig 2)
RAB-11+ apical recycling endosomes loss	no	yes	yes	yes	yes	yes (Fig 2)
lysosomal abnormalities	no	Enlarged (auto)lysosomes	Enlarged (auto)lysosomes	high number of lysosomes	enlarged lysosomes	enlarged and high number of lysosomes (Fig 2)
STX3 localization	apical membrane	Subapical vesicle and MVIs	reduced/absentprote in level	subapical vesicle and MVIs	diffuse in cytoplasm	UNC-64 (STX3 ortholog) membrane accumulation (Fig 3)
Brush border proteins defects (ERM-1, ACT-5)	strong in brush border	Reduced brush border signal, MVIs positive	presence of dot- and ring-like structures	reduced brush border, MVIs stained; variable penetrance and severity	reduced brush border, cytoplasmic foci and MVIs stained	reduced brush border, presence of MVI structures (Fig 1, 4, 5, 6)

Supplementary Table S4: *C. elegans* strains used in this study

Srain name	Genotype	Reference
MCP59	*bab59[erm-1::mNG^SEC^3xFlag] I*	This study
MCP64	*erm-1(bab91[erm-1::wrmSc^3xFlag]) I*	This study
FL369	*fgEx13[perm-1::erm-1::gfp + rol-6 (su1006)] ; jyIs17 [vha-6p::mcherry::act-5, ttx-3p::RFP]*	This study
FL316	*dfEx3 [vha-6p::gfp::cdc-42 + rol-6 (su1006)]; unc-119(ed3)III; mcIs46 [dlg-1::rfp+unc-119(+)]*	This study
KK1248	*par-6(it319[par-6::GFP]) I*	CGC
KK1228	*pkc-3(it309[GFP::pkc-3]) II*	CGC
GK446	*unc-119(ed3) ; dkIs259[Pact-5-GFP-snap-29 ; Cb.unc-119(+)]*	Sato et al., 2011
FL373	*pkc-3(it309[GFP::pkc-3]) II; erm-1(bab91[erm-1::wrmSc^3xFlag]) I*	This study
MCP113	*bab113[wrmSc^3xFlag::pgp-1] IV*	This study
KWN117	*rnyEx60 [pELA2 (vha-6p:::vha-6::mCherry) + myo-3p::GFP + pCL1 (pha-1+)]*	V. Gobel
FL375	*rnyEx60 [pELA2 (vha-6p:::vha-6::mCherry) + myo-3p::GFP + pCL1 (pha-1+)]; pwIs69 [vha6p::GFP::rab-11 + unc-119(+)]*	This study
KWN246	*pha-1(e2123) III, rnyEx133[opt-2(aa1-412)::GFP) + pha-1(+)]*	CGC
FL368	*bls5[chc-1p::gfp::chc-1 + rol-6(su1006)]; jyls17 [vha-6p::mcherry::act-5, ttx-3p::RFP]*	
MCP91	*unc-64(bab91[wrmSc^3xFlag ::unc-64]) III*	This study
RT258	*pwIs50 [lmp-1::GFP + Cbr-unc-119(+)]*	CGC
RT327	*pwIs72 [vha-6p::GFP::rab-5 + Cbr-unc-119(+)]*	CGC
RT476	*pwIs170 [vha6p::GFP::rab-7 + Cbr-unc-119(+)]*	CGC
RT525	*pwIs206 [vha6p::GFP::rab-10 + Cbr-unc-119(+)]*	CGC
RT311	*pwIs69 [vha6p::GFP::rab-11 + unc-119(+)]*	CGC
VJ268	*fgEx12[pact-5::act-5::gfp]*	Zhang et al., 2012
FL376	*pwIs50 [lmp-1::GFP + Cbr-unc-119(+)]; erm-1(bab91[erm-1::wrmSc^3xFlag]) I*	This study
GK385	*unc-119(ed3) ; dkIs218[Popt-2-GFP-syn-1 ; Cb.unc-119(+)]*	Sato et al., 2011
FS254	*slcf-1(tm2258); Exfs254[slcf-1::gfp]*	Mouchiroud et al., 2010
DA2123	*adIs2122 [lgg-1p::GFP::lgg-1 + rol-6(su1006)]*	CGC